Two-Phase CFD Model of the Bubble-Driven Flow in the Molten Electrolyte Layer of a Hall–Héroult Aluminum Cell

YUQING FENG, M. PHILIP SCHWARZ, WILLIAM YANG, and MARK COOKSEY

A two-phase computational fluid dynamics (CFD) model has been developed to simulate the time-averaged flow in the molten electrolyte layer of a Hall–Héroult aluminum cell. The flow is driven by the rise of carbon dioxide bubbles formed on the base of the anodes. The CFD model has been validated against detailed measurements of velocity and turbulence taken in a full-scale air–water physical model containing three anodes in four different configurations, with varying inter-anode gap and the option of slots. The model predictions agree with the measurements of velocity and turbulence energy for all configurations within the likely measurement repeatability, and therefore can be used to understand the overall electrolyte circulation patterns and mixing. For example, the model predicts that the bubble holdup under an anode is approximately halved by the presence of a slot aligned transverse to the cell long axis. The flow patterns do not appear to be significantly altered by halving the inter-anode gap width from 40 to 20 mm. The CFD model predicts that the relative widths of center, side, and end channels have a major influence on several critical aspects of the cell flow field.

I. INTRODUCTION

REDUCTION of alumina in the Hall–Héroult aluminum cell requires large amounts of electrical energy (about 13 kWh kg^{-1}), and also involves consumption of carbon anodes. This means that the process results in the emission of large amounts of carbon dioxide, particularly if the electrical power is generated from fossil fuels.

In the Hall–Héroult cell, current is passed between carbon anodes and a horizontal cathode, above which lies a layer of molten aluminum formed by the reduction process. The ends of the anodes are submerged in a layer of electrolyte (commonly referred to as "bath") consisting of molten cryolite into which alumina is dissolved. The process is carried out at a temperature of approximately 1243 K (970 °C), with a crust of solidified cryolite (the "ledge") intentionally formed on the walls of the cell to protect them from the cryolite. Bubbles of gas (primarily CO_2) form on the lower faces of the anodes as a result of electrochemical reduction; they slide along the anodes until they reach a vertical channel in which they can rise to the surface of the electrolyte, generating turbulent flow in the electrolyte as they do so.

It should be possible to reduce the energy requirement towards the minimum theoretical requirement by reducing unnecessary energy losses, as detailed in the descriptions of the design and operation of the Hall–Héroult cell in the literature, e.g., Grjotheim and Welch,[1] and in a recent review of energy constraints on cell design and operation.[2] Many of the losses relate to issues in the electrolyte in which the alumina reduction is carried out: for this reason, a predictive mathematical/numerical model of electrolyte behavior should assist in making design and operational improvements to improve efficiency. Some of the potential areas for improvement are given below.

1. If the thickness of the electrolyte layer could be decreased, the ohmic drop across it would be reduced. However, magnetohydrodynamic waves on the metal-bath interface impose a lower limit on the electrolyte layer thickness if shorting is to be avoided.
2. The bubble layer beneath the anodes increases the ohmic drop across the electrolyte because of the locally increased current density resulting from the reduced area through which the current can pass in the bubble layer. This additional bubble voltage could potentially be reduced if the bubble holdup under the anodes could be decreased. On the other hand, the bubbles are also beneficial since they generate turbulent flow in the electrolyte as they rise to the surface, and this flow is crucial to alumina distribution and maintaining thermal conditions in the cell.
3. Current efficiency is affected by numerous factors, many of which relate to the hydrodynamics in the electrolyte. For example, migration of carbon dioxide species to regions in which aluminum is present will lead to back reaction, reducing current efficiency.
4. Improved cell control and reduced variability can also have an effect on energy efficiency. Issues such as

YUQING FENG, Senior Research Scientist, M. PHILIP SCHWARZ, Honorary Fellow, WILLIAM YANG, Principal Research Scientist, and MARK COOKSEY, Group Leader, are with the CSIRO Mineral Resources Flagship, Melbourne, Australia. Contact e-mail: Phil.Schwarz@csiro.au

temperature control, formation of a stable ledge of frozen cryolite, minimization of anode effects, and improved alumina feeding are all strongly affected by bath hydrodynamics.

Electrolyte flow in the bath phase has a strong influence in all these areas; it is apparent therefore that an improved understanding of, and ability to control, bath hydrodynamics should assist in improving overall cell operation and in particular energy efficiency. Unfortunately, bath dynamics is not easily understood as it is the result of several complex coupled transport phenomena: bubble formation and the resultant gas-driven recirculation, thermal transport and the interaction with ledge freezing and melting, alumina transport, electrolyte chemistry, and current distribution. A detailed predictive three-dimensional numerical model of bath hydrodynamics will be invaluable in this endeavor, given the difficulty of taking detailed hydrodynamic and bubble voidage measurements in operating cells and the impossibility of constructing exact physical analogs (or models) of a cell at room temperature, despite the usefulness of water models. In principle, numerical flow models are ideal for accounting for the interactions between multiple transport phenomena because of the iterative nature of the solution procedures used—iteration continues until the multiple equations governing the various transport processes are all satisfied. This paper describes the development and validation of a multi-phase (gas–liquid) computational fluid dynamics (CFD) model of a multi-anode cell which can be the core of a numerical model incorporating all these transport processes.

II. PREVIOUS WORK

There have been few reported flow studies in real aluminum electrowinning cells because of severe technical difficulties. The first reported flow measurement was by Nikitin et al.[3] who found that velocities near the underside of the anode (driven by bubbles sliding from the center towards the periphery of the anode) were about 0.35 m s^{-1}, whereas the flow near the surface of the cathode was about 0.04 m s^{-1} in the opposite direction. This picture of the bath flow magnitude and pattern in the anode–cathode gap (ACG) beneath anodes has been confirmed by subsequent work. Kobbeltvedt and Moxnes,[4] estimating flow velocities using a temperature technique, found expected horizontal flow patterns in center and side channels with speeds in the range 0.02 to 0.08 m s^{-1}. The observed asymmetry suggests that MHD forces are important as well as bubble-driven effects.

Most experimental work on electrolyte hydrodynamics has used air–water models. Dernedde and Cambridge[5] employed visualization in a two-liquid (water-organic) simulation of the electrolyte-metal system, together with air injection: bead movement was used to quantify recirculation in the side channel which was fitted with a side-freeze profile. Thermal natural convection near the freeze layer was shown to be negligible

compared with bubble-driven flow, and waves were found to be excited at the "bath-metal" interface by the bubbling.

Solheim et al.[6] studied a full-scale two-dimensional air–water slice model. They used tracer movement under the anode to infer maximum velocities of about 0.2 to 0.3 m s^{-1} near the anode (towards the channel), with a maximum of about 0.06 m s^{-1} away from the channel near the metal interface. Despite the quantitative uncertainty, reliable conclusions could be made that the water velocity depends mostly on anode base inclination angle and gas flow rate, with little dependence on immersion depth or electrolyte layer thickness (provided it was more than about 30 mm). The authors conclude that the flow beneath the anode is largely decoupled from the flow in the vertical channels beside the anodes.

Chesonis and LaCamera[7] utilized a full-scale oil–water–air model to simulate both bath and metal phases with the effect of the Lorentz force on recirculation simulated in an approximate way by external pumping. Laser Doppler velocimetry (LDV) measurements in the anode–anode gap showed large fluctuations associated with pulsing of the two-phase flow most likely caused by bubble release coupled to interface oscillation; the authors pointed out that there is an associated wave on the bath-metal interface in regions below anode–anode gaps which could be a limiting factor on electrolyte layer thickness. They also found that the time for simulated alumina mixing (20 to 30 minutes for typical current densities) was controlled by gas-driven flows, with flows due to electromagnetic forces being much less important.

LDV measurements of velocity in the ACG of a water model cell were first reported by Shekhar and Evans,[8] confirming the previous estimated magnitudes in the ACG, with speeds of 0.06 to 0.08 m s^{-1} near a flat anode and as high as 0.14 m s^{-1} near an anode inclined at 11.1 deg; higher speeds were measured for water-butanol mixtures in which the surface tension was lowered.

The flows in the side and center channels were studied by Chen et al.[9] using a heat transfer probe. The measurements provide a clear picture of speed increasing towards the top surface in the channels, and generally being higher at the middle of the vertical faces of the anodes compared to near the corners.

The first comprehensive fluid dynamic measurements were made by Cooksey and Yang[10] using particle image velocimetry (PIV) on a full-scale three-anode water model. They showed that the addition of slots had a significant effect on flow and turbulence distribution.

In addition to the liquid flow measurements described above, there have also been several studies relating to size, shape, and speed of bubbles formed under the anodes.[11–14]

With regard to numerical modeling, the first published two-phase CFD model of bath flow in an aluminum cell,[6] developed by Johansen,[15] used the Fluent code in which the bubble phase is simulated with Lagrangian particle tracking and ignores gas volume effects; the modeling was limited to two dimensions because of computational speed constraints at the time. The model results agreed with water modeling work,

and also showed that metal flow of the magnitude generated by magnetic forces would not significantly influence electrolyte flows through interfacial stresses, thereby validating the neglect of the metal phase in electrolyte hydrodynamics studies.

Three-dimensional modeling for a single anode carried out by Purdie et al.,[12] using essentially the same technique as Johansen's, showed the basic flow pattern consisting of recirculation in the center and side channel and outflow in the inter-anode gap (or slot). These results were combined with a connected-tanks model to predict mixing times (of order 10 to 20 minutes) which were in reasonable agreement with water model tracer mixing experiments. Bilek et al.[16] used this model to delineate the overall flow patterns expected in an entire multi-anode cell. Bubble-driven forces were shown to be more important than MHD forces by a factor of about 10, though no validation of the model was given. The same technique has been used in a simple two-dimensional model to investigate likely mass transfer at the metal-bath interface.[17]

The first detailed validation of a three-dimensional CFD model was conducted by Feng et al.[18,19] using an Eulerian method for the bubble phase which accounts for bubble volume. The model predicts recirculation in the side channels, as observed, and the complex flow pattern measured in the ACG beneath the horizontal surface of the anodes was well predicted.[20] The model has been used to investigate alumina mixing and bubble holdup in industrial multi-anode cells.[21]

Gas-driven bath flow has been included in a three-phase model (encompassing both metal and bath and MHD effects) of an entire 36-anode cell by Li et al.[22] Detailed results of the bath flow are not given and the computational mesh is relatively coarse given the large number of anodes and the complex physics involved.

The literature has shown that water models, though fortuitously similar in many respects to the bath phase of a cell, will never be exactly similar, and furthermore are time consuming to build and measure. CFD models therefore provide an ideal tool for studying bath hydrodynamics. Of course the numerical models still need to be validated, and it is sufficient to use air–water models for this purpose, because although not exactly similar, they capture the essential physics. CFD models are fundamentally based so, once validated, can be used with confidence for values of density, viscosity, surface tension, contact angle, etc., more characteristic of real cells. Furthermore, they can be used to investigate potential design modifications, other operating conditions, and even advanced designs such as vertical anode arrangements.

III. CFD MODEL EQUATIONS

A. *Two-Fluid Model Equations*

The primary external forces driving the bath phase of an aluminum cell are gravity (manifest through buoyancy on bubbles) and the Lorentz force. The second of these is not considered in this paper which is concerned with validation of the CFD model against water model data in which the Lorentz force does not occur, however, it is relatively straightforward to add the Lorentz force as a body force in a model of an actual cell once the current density and magnetic field have been solved. It has been shown[12] that the Lorentz force is about an order of magnitude smaller than the bubble-related buoyancy force in the bath phase.

Considering the effective density differences involved, it is straightforward to show that the driving force for thermal natural convection in aluminum cells will be orders of magnitude smaller than the driving force for bubble buoyancy-generated flows.

Given the fluid speeds found in previous work, the Reynolds number for flow in the vertical channels is of order 5000, implying that the flow is most likely turbulent, as observed in water models. Although no information exists for the critical Reynolds number for transition for such complex geometries as found in cells, the presence of bubbles will certainly lead to transition at lower Reynolds numbers than would otherwise occur in an undisturbed single-phase flow in the same geometry. To properly account for turbulence, therefore, the CFD model uses the Reynolds averaging technique, in which equations are derived that govern the flow averaged over the intrinsically unpredictable random turbulent fluctuations. The k–ε form of the closure has been used in the present work with the standard constants, and with additional source terms to account for turbulence generated in the bubble wakes.

The motion of bubbles and their interaction with the liquid phase is taken into account using the two-fluid model[23] (applied to bubbly flows by Schwarz and Turner[24]) which solves coupled Eulerian equations for the phases derived by rigorous averaging analogous to Reynolds averaging. The equations solved are: Conservation of mass:

$$\nabla \cdot (\gamma_\alpha \rho_\alpha \mathbf{U}_\alpha) = 0. \qquad [1]$$

Conservation of momentum:

$$\nabla \cdot (\gamma_\alpha (\rho_\alpha \mathbf{U}_\alpha \otimes \mathbf{U}_\alpha)) \\ = \gamma_\alpha \nabla p + \nabla \cdot \left(\gamma_\alpha \mu_\alpha \left(\nabla \mathbf{U}_\alpha + (\nabla \mathbf{U}_\alpha)^T \right) \right) + S_\alpha + \mathbf{M}_\alpha, \qquad [2]$$

where γ_α is the volume fraction of phase α (either gas or water), ρ_α and $\mathbf{U}_\alpha$ are the density and vector velocity for phase α, and p and μ_α are the pressure and effective viscosity. The term S_α describes momentum sources due to external body forces, e.g., buoyancy and electromagnetic force (though the electromagnetic force is not included in the water flow model). The term $\mathbf{M}_\alpha$ describes the interfacial momentum transfer between phases and can include the drag force, lift force, virtual mass, wall lubrication force, inter-phase turbulent dispersion force, etc. The effective viscosity is the sum of molecular (dynamic) viscosity (μ_0) and turbulent viscosity (μ_t).

Note that turbulence and bubble motion may be coupled to other unsteady phenomena in the bath such

as waves on the surface. In this work, we seek a time-averaged description of the flow, and hence solve the steady form of the averaged momentum equations.

A commercial CFD code,[25] CFX, has been used to obtain a solution of these equations using iterative techniques.

B. Turbulence Model

The k–ε two-equation model is applied for the liquid phase since, being the continuous phase, this is the phase in which eddies originate. The turbulence eddy viscosity is calculated as

$$\mu_{\rm tl} = c_\mu \rho_{\rm l}\big(k^2/\varepsilon\big). \qquad [3]$$

The constant c_μ is the k–ε turbulence model constant (default value 0.09), and k and ε are turbulence kinetic energy and turbulence dissipation rate, respectively. Gas bubbles are dragged around by energetic eddies to an extent determined by bubble size, so the turbulence eddy viscosity for the gas phase is expected to be well approximated by

$$\mu_{\rm tg} = c_\mu \frac{\rho_{\rm g}}{\rho_{\rm l}}\frac{\mu_{\rm tl}}{\sigma}. \qquad [4]$$

The parameter, σ, is a turbulent Prandtl number relating the dispersed phase kinematic eddy viscosity to the continuous phase kinematic eddy viscosity, and depends on the extent to which bubbles respond to turbulent eddies in the liquid phase (or Stokes number): it takes the limiting value of unity for very small bubbles. The transport equations for k and ε are assumed to take a form similar to the single-phase closure[24]:

$$\nabla \cdot \left(\gamma_\alpha(\rho_{\rm l}\mathbf{U}_{\rm l}k) - \left(\mu + \frac{\mu_{\rm tl}}{\sigma_k}\right)\nabla k\right) = \gamma_\alpha(P_k - \rho_{\rm l}\epsilon) + S_k$$

$$[5]$$

$$\nabla \cdot \left(\gamma_\alpha(\rho_{\rm l}\mathbf{U}_{\rm l}\varepsilon) - \left(\mu + \frac{\mu_{\rm tl}}{\sigma_\varepsilon}\right)\nabla \varepsilon\right) = \gamma_\alpha \frac{\varepsilon}{k}(C_{\epsilon 1}P_k - C_{\epsilon 2}\rho_{\rm l}\epsilon) + S_\epsilon,$$

$$[6]$$

where $C_{\varepsilon 1}$, $C_{\varepsilon 2}$, σ_k, σ_ε are turbulence model constants, default values being 1.44, 1.92, 1.0, and 1.3 respectively. P_l is the turbulence production term: $P_k = 2(\mu_{\rm tl}/\gamma_{\rm l})E_{ij}E_{ij}$, where E_{ij} is the rate of deformation tensor, and the summation convention applies over the indices i and j. The terms S_k and S_ϵ represent sources for k and ε, respectively, primarily in this case from interactions with bubbles.

C. Bubble-induced Turbulence

Bubbles rising in the molten bath give rise to increased turbulence of the liquid phase, known as bubble-induced turbulence. Various models have been proposed in the literature to account for this mechanism, with the two most widely accepted being modifying turbulence eddy viscosity by adding a bubble-induced

term,[26] and adding a source of bubble-induced turbulent kinetic energy. Bubble-induced turbulence is very case dependent and is still an active area of research, so there is not yet agreement on a universal source term for general use.[27] Most of the published research relates to vertical pipe bubbling flow which will be different from less confined flow.

Following Kataoka and Serizawa,[28] the source term for turbulence energy is taken to be proportional to the work done by the drag force, which is the product of the drag force, $F_{\rm D}$, and the slip velocity between the two phases:

$$S_k = C_k \mathbf{F}_{\rm D} \cdot \big(\mathbf{U}_{\rm l} - \mathbf{U}_{\rm g}\big). \qquad [7]$$

Note that this expression, which differs from the term previously used by Feng *et al.*,[20] has a sound theoretical basis, and, as will become clear later in the paper, results in predicted values of turbulence intensity in good agreement with experiment. To enhance convergence, in regions where bubbles rise freely under buoyancy, the term is calculated as

$$S_k = C_k \rho_{\rm l}g\gamma_{\rm g}\big|\mathbf{U}_{\rm g} - \mathbf{U}_{\rm l}\big| \qquad [8]$$

where g is the acceleration due to gravity. This is a close approximation given that bubbles quickly reach terminal velocity where drag and buoyancy balance. This approximation is not used in the ACG.

The corresponding source term in the ε-equation is modeled as usual[27] by

$$S_\epsilon = \frac{C_\varepsilon}{C_k}\frac{\epsilon}{k}S_k. \qquad [9]$$

The constants C_k and C_ε are coefficients for bubble-induced turbulence kinetic energy and energy dissipation respectively.

D. Bubble-induced Turbulent Dispersion Force

A turbulent dispersion force is proposed in the literature to account for the diffusion of bubbles due to the random influence of turbulent eddies in the liquid. The Favre averaged turbulence dispersion force model[29] has been used in this study.

The force is given as

$$\mathbf{M}_{\rm l}^{\rm TD} = -\mathbf{M}_{\rm g}^{\rm TD} = -C_{\rm TD}C_{\rm d}\frac{v_{\rm tl}}{\sigma_{\rm tl}}\left(\frac{\nabla\gamma_{\rm g}}{\gamma_{\rm g}} - \frac{\nabla\gamma_{\rm l}}{\gamma_{\rm l}}\right), \qquad [10]$$

where $C_{\rm d}$ is the drag coefficient, $v_{\rm tl}$ is the kinematic turbulent viscosity of the liquid, and $\sigma_{\rm tl}$ is the relevant Prandtl number. A universally applicable value of the coefficient, $C_{\rm TD}$, cannot be determined theoretically or from previous experimental studies.[30] In this work, physical measurements are used to determine appropriate values on a trial-and-error basis. Considering that bubble-induced turbulence is suppressed beneath anodes (in the ACG) and that bubbles grow to large sizes there, the value in this region is set to a small value. Table I lists the values used for this study.

Table I. Coefficients for Bubble-induced Turbulence

	C_k	C_ε	C_{TD}
ACG	0.2	0.2	0.025
Other regions	0.2	0.2	0.2

E. *Boundary Conditions*

The boundary conditions are set as the following:

- a gas inlet to the computational domain on the bottom surface of the anode representing gas generation by reduction of alumina;
- a gas outlet on the top surface of the liquid pool (assumed to be flat) through which gas leaves the bath at the rate it arrives from below (*i.e.*, the so-called "degassing condition");
- "walls" on the other solid boundaries (*i.e.*, no slip for water and free slip for air).

The assumption of a flat horizontal top surface of the liquid pool is clearly an approximation—wave motion will be associated with bubble bursting and turbulence. However the assumption is appropriate given that the present work seeks to determine the time-averaged flow in a pragmatic way suitable for design purposes, and surface motion is unlikely to significantly affect the average behavior of the bath.

The present model is set up for validation purposes for a water model, which does not contain a simulated metal (aluminum) phase. The base of the tank (simulating the bath-metal interface) is the lower boundary of the domain, and is a flat, horizontal boundary with zero-slip condition. When applied to modeling the bath phase of a real cell, this condition could be modified if information on the metal phase is available, but in any case, metal velocities are known to be smaller in magnitude than bath velocities.[6]

F. *Bubble Size*

Bubbles grow by coalescence on the under-surface of anodes to large highly flattened shapes: an equivalent spherical diameter is estimated to be 0.07 m on the basis of observation of the water model. Bubbles that release into the side and center channels are subject to breakage in the turbulent plumes. The Weber number

$$\text{We} = \rho d (\Delta V)^2 / T \qquad [11]$$

can be used to determine the size to which bubbles are broken. It is expected that the velocity fluctuation in the plume, ΔV, can be approximated as 20 pct of the plume velocity which is on average 10 mm s^{-1}. Taking the surface tension, T, to be 0.07 N m^{-1} gives a bubble size, d, of approximately 40 mm for a critical Weber number of 2.6.[31]

Momentum exchange through drag force is calculated according to the Schiller-Naumann drag correlation,[32] used as a generic correlation for equivalent bubble diameter given the range of complex bubbly flow regimes present in the cell. For example, little information exists on drag forces for highly flattened bubbles

moving under a horizontal surface, nor are there predictive models for the size of such bubbles at each point on the lower surface of the anode. In future extensions of the model, available information[11,13,33] will be incorporated into the model. Bubbles that rise in the inter-anode gaps where break-up is suppressed are assumed to be the same size as those under the anode.

G. *Enhanced CFD Model*

The CFD model equations described in the subsections above are similar to those previously published,[20] but with different values of bubble size and a different expression for bubble-induced turbulence. This expression has a sounder theoretical basis, and, as we will see, results in predicted values of turbulence intensity much closer to the measured values. This model will be henceforth referred to as the standard model. An enhanced model, incorporating the modification described below, has also been run for each configuration.

Bubble size in the center and side channels and in the inter-anode gap is larger than the computational cell dimension, particularly in the direction normal to the anode wall. Gas escaping into the channels from the layer below the anodes preferentially moves into the row of cells adjacent to the cell wall because of the strong upwardly oriented buoyancy force, and the relatively low velocity of bubbles along the anode base prior to escape. In reality, the strong surface tension force ensures that each bubble is spread out over a horizontal distance of order the bubble size, but this effect is not accounted for in the standard multi-fluid equations. The enhanced model allows for this surface tension effect by introducing an equivalent dispersion force at the entrances to the channels. The form of the dispersion force is taken to be the same as in Eq. [10], but with the coefficient taken as that required to generate an initial plume width equal to the required bubble size. For the side, center, and end channels, $C_{TD} = 60$ is applied over a vertical height of 30 mm at the base of the anodes.

IV. VALIDATION EXPERIMENT MODELED

The CFD model developed for simulation of aluminum reduction cells has been validated using data taken on the air–water model described by Cooksey and Yang.[10] The physical model, illustrated in Figure 1, consists of three anodes of a scale typical of a modern pre-bake cell, though the dimensions and conditions do not correspond to any actual operation. The physical model was constructed in Perspex to facilitate particle image velocimeter (PIV) measurements of velocity, as described in detail by Cooksey and Yang.[10] Measurements were typically averaged over 100 to 200 seconds to obtain the time-averaged data used in this paper. Each anode is dimensioned 1300 mm × 650 mm × 600 mm with 160 mm of the anode submerged; other experimental conditions for the experiments being simulated in this paper are
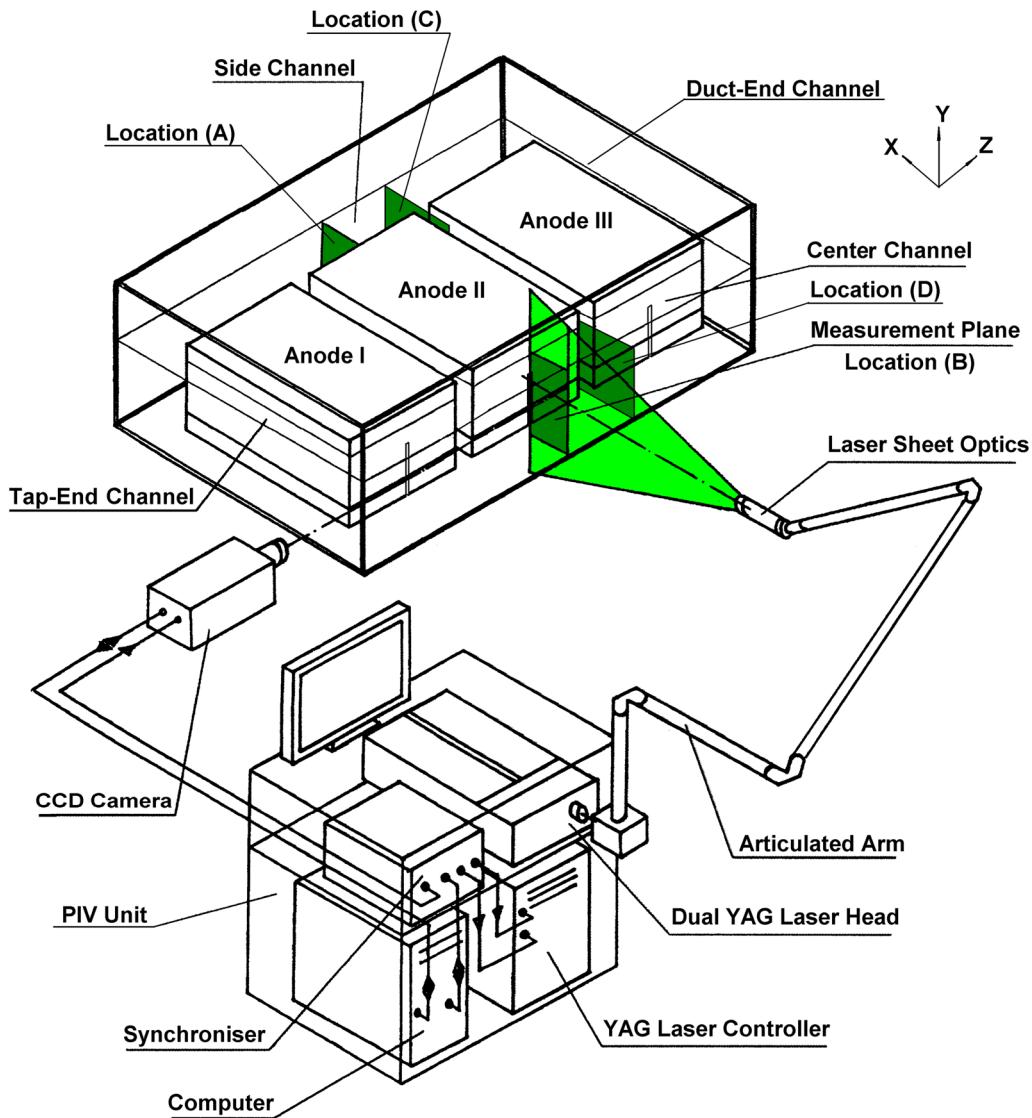
Fig. 1—Three-anode physical model, showing arrangement of PIV measurement for vertical planes.

	Configurations 1, 3	Configurations 2, 4
ACD (anode–cathode distance):	40 mm	40 mm
Anode slope:	0 deg	0 deg
Tap-end channel width:	160 mm	120 mm
Duct-end channel width:	40 mm	40 mm
Side channel width:	240 mm	240 mm
Center channel width:	120 mm	120 mm
Inter-anode gap width:	40 mm	20 mm
Liquid depth:	200 mm	200 mm
Gas flow rate per anode (Configs 1, 2)	120 L min^{-1}	120 L min^{-1}
Gas flow rate per anode (Configs 3, 4)	103 L min^{-1}	103 L min^{-1}

Configurations 3 and 4 include a vertical slot through the middle anode, in the direction of the long dimension of the anode. The slot is 15 mm wide and cuts through the entire submerged part of the anode, effectively dividing it into two smaller anodes separated by a channel. This configuration represents the condition that usually applies for new anodes. As the anode wears, the height of the slot reduces so that the top of the slot is submerged by an ever greater amount until the slot is entirely worn away. The effectiveness of a worn slot could be analyzed using the present model.

The dominant force driving flows in the electrolyte is bubble buoyancy, and the experimental arrangement is designed particularly to achieve similarity in this regard. Similarity of flow is thus achieved if the buoyancy force per unit mass of liquid

$$\left(\rho_l - \rho_g\right)g\alpha/\rho_l \approx g\alpha \qquad [12]$$

is the same in the physical model as that in the cell. The local gas volume fraction, α, will be the same in the two cases if both the volumetric flow rate of gas and the bubble properties (size, shape, *etc.*) are the

same. Stoichiometry for the electrochemical reaction implies that the volume flow of gas in a cell is given by[34]

$$q = q_0 I, \qquad [13]$$

where $q_0 = 2.64 \times 10^{-7}$ m^3 s^{-1} A^{-1} at 1243 K (970 °C). Thus, the flow rate used in the water model, 120 L min^{-1}, at one atmosphere and room temperature, corresponds to a current of 7.6 kA per anode.

The kinematic viscosity should ideally be of the same order in model and cell to ensure that flow is in the same regime (*i.e.*, turbulent) and that the boundary layers are of comparable thickness: the values are 8.9×10^{-7} m^2 s^{-1} for water and 1.1×10^{-6} m^2 s^{-1} for cryolite[6] which are indeed, fortuitously, very close. Finally, for bubble size and shape to be similar, kinematic surface tension (σ/ρ) between gas and liquid is the critical parameter: this is indeed approximately the same for water/air and cryolite/CO_2 systems.[11,33]

Geometric idealizations in the water model include square anode edges/corners and square profile side channel (*i.e.*, no ledge). It is expected that these simplifications will not change the general nature of the flow pattern, so the experimental data are suitable for the purpose of validation of the CFD model; since the model is fundamentally based, it can then be used with confidence to simulate more realistic geometrical details and potential design modifications. Note that the physical model simulates anodes on only one side of the center channel, with the tank wall representing a symmetry boundary; although flows in the model center channel may not for this reason be entirely representative of flows in the real cell, the data are certainly adequate for model validation.

V. RESULTS

A. *Configuration 1: Case with 40 mm Inter-anode Gap Width and No Slot*

The CFD model was first run for the case of 40 mm inter-anode gap width and no slot. The rising gas bubbles drive a recirculating vortex flow that extends along the entire length of the center and side channels. The flow on a plane through the center of the middle anode is shown in Figures 2(a) and (b) at the side and center channels, respectively; while Figures 2(c) and (d) show cross sections through the middle of the inter-anode gap at the side and center channels, respectively (see Figure 1 for location of measuring planes). In each case, the PIV-measured field is given at the top, and the enhanced CFD model at the bottom. In Figures 2(a) and (b), the predictions of the standard model are also shown. The model and experimental flow patterns are very similar, although the vortex center is slightly shifted for the side channel. The standard and enhanced model predictions of flow pattern are almost identical. It must be remembered that the flow vectors are time-averaged, and that the flow field at any instant has superimposed turbulence.

The predicted turbulence levels are similar to the measured values, with the enhanced model giving excellent quantitative agreement, given the uncertainties in the k and ε equations related to the complex bubble-turbulence interactions. The enhanced model gives lower values of turbulence energy in the plume than the standard model because the more realistic bubble plume width produces lower velocity peak voidage and hence lower bubble-induced turbulence.

Note that turbulence fluctuations were measured in only two velocity components, namely u' and v'. Except in boundary layers very close to walls, turbulence is generally close to isotropic, so the total kinetic energy of turbulence can be estimated to be

$$k = \frac{3}{4}\left(\overline{u'^2} + \overline{v'^2}\right). \qquad [14]$$

This is 1.5 times larger than the value plotted by Cooksey and Yang[10] which is the energy in the measured components only. The values plotted in Figure 2 are three-component values with experimental values estimated using Eq. [14].

In Figures 2(a) and (b) (planes A and B), the experimental results show much lower levels of turbulence underneath the anode compared with the CFD results. However, only a small fraction of the ACG was measured (that part near the edge of the anode), and the measurement of turbulence under the anodes is further complicated by high levels of voidage under the anodes which must make unbiased velocity measurement more difficult; the fact that only two components of velocity (hence velocity fluctuation) are measured; the fact that turbulence under the anodes will most likely be highly anisotropic given that it will be dominated by bubble movement (especially given the large horizontal extent of the flattened bubbles). Furthermore, it will be seen below that for Configuration 2, the measured turbulence levels under the anode on planes A and B are very similar to that given by the model. Yet the only difference between Configurations 1 and 2 is that the inter-anode gap in halved: it is hard to understand how this change could make such a large change to the turbulence level in a region of the cell so far away from the gap. This apparent inconsistency will be further discussed below.

Quantitative comparison between measured and predicted velocities is given in Figures 3 and 4. Vertical and horizontal velocity components are plotted on traverses at three heights through both center and side channels. Figure 3 gives results for the transverse plane through the middle of the middle anode, while Figure 4 gives results for the plane through the middle of the inter-anode gap, as shown in Figure 1. Agreement in most cases is better than 10 mm s^{-1}. The only region where the difference between model and measured velocity is greater than this is the plume adjacent to the side of the anode where the upward velocity is overestimated. The predicted upward flow in the middle of the side channel is also slightly lower than measured.

Agreement between model and experiment is generally good, but difficult to quantify because uncertainty
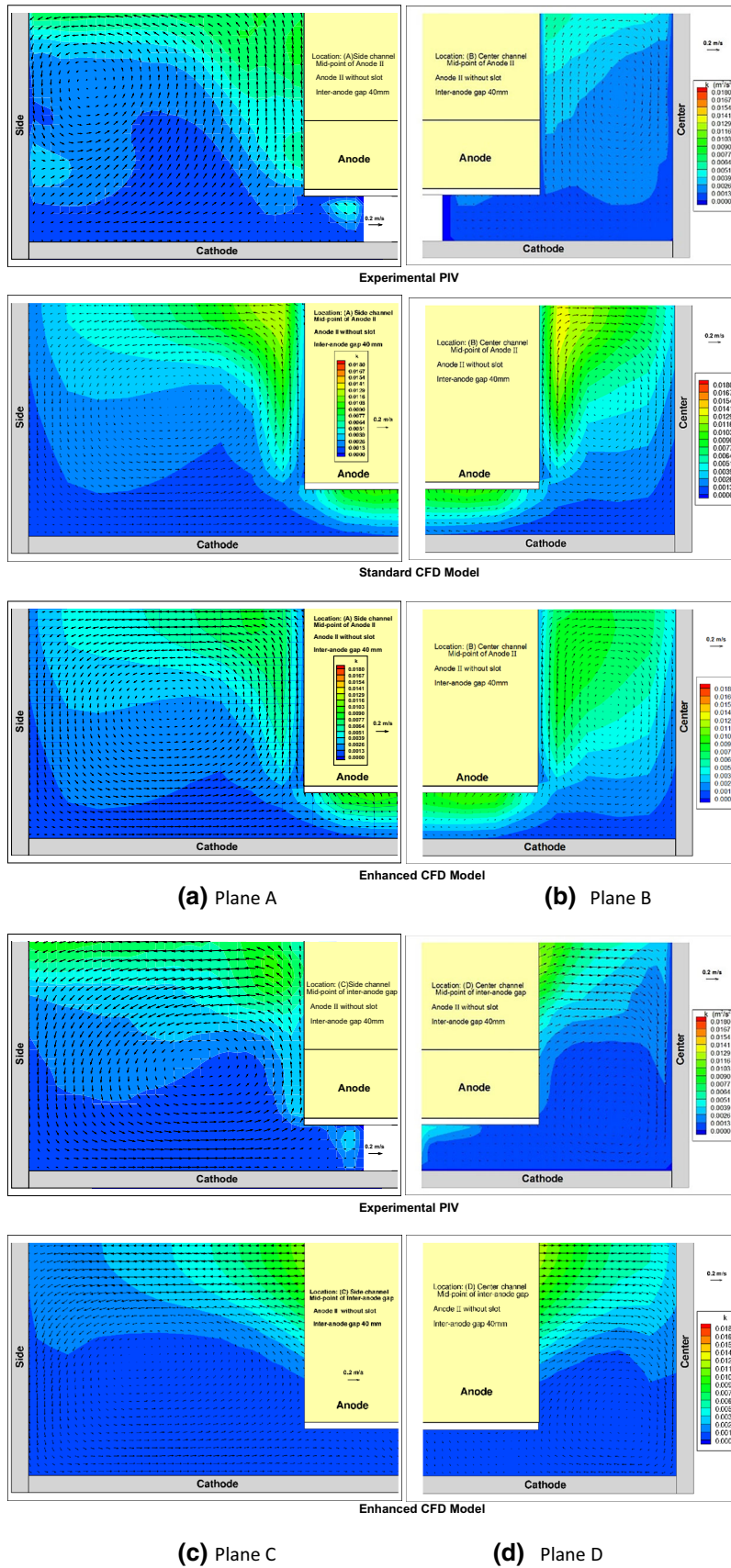
(a) Plane A **(b)** Plane B

(c) Plane C **(d)** Plane D

Fig. 2—Measured and predicted liquid velocity and turbulence for configuration 1 (Anode II without slot, 40 mm inter-anode gap) at four locations: (*a*) A; (*b*) B; (*c*) C; (*d*) D. In each case, PIV measurements (top) are compared with CFD model (lower).
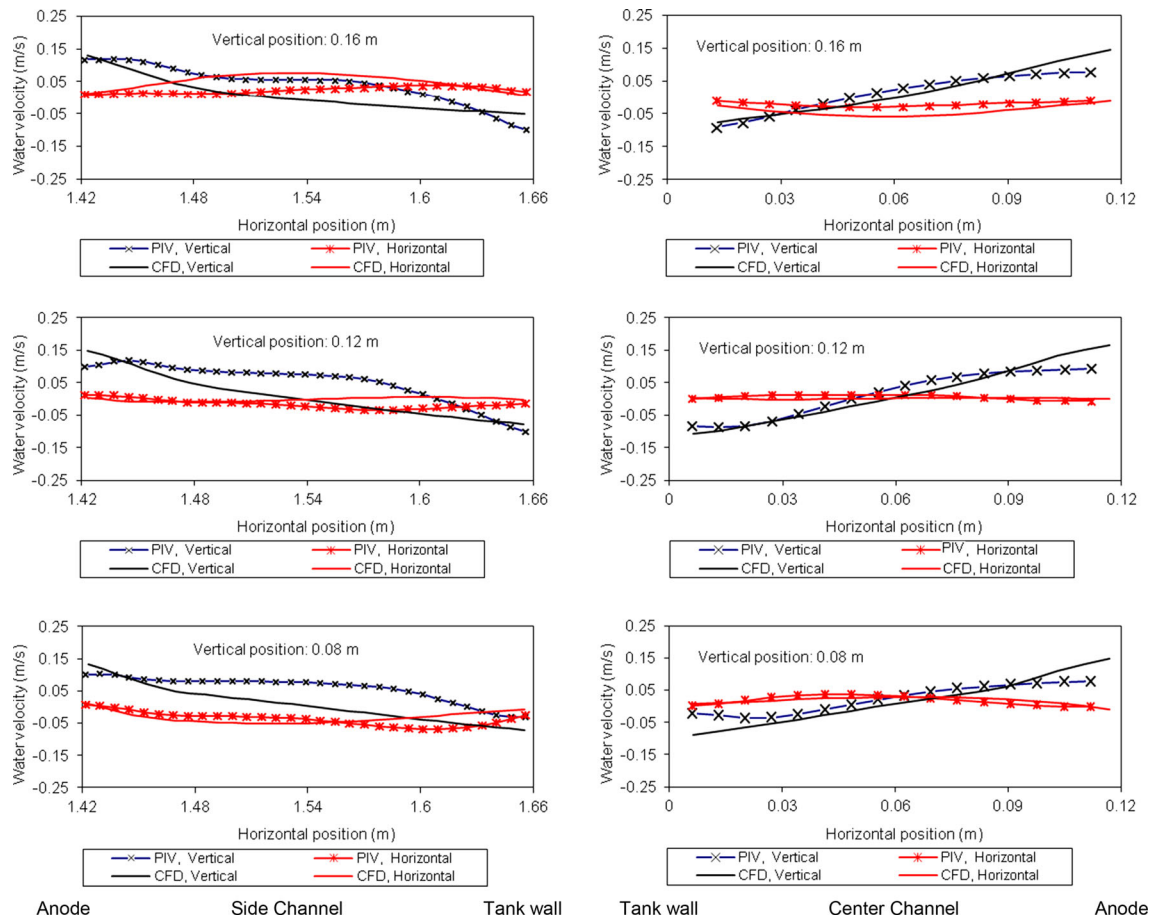
Fig. 3—Comparison for Configuration 1 between PIV measurement and CFD simulation of water velocity on mid-anode plane in side channel (location A) and center channel (location B) shown on left side and right side respectively.

in the measurement data is hard to assess. PIV measurements are in principle very accurate, and precautions were taken by Cooksey and Yang[10] to guard against issues that can be problematic for PIV of bubbly flows, as pointed out by Delnoij et al.[35] Therefore individual velocity measurements should be accurate to better than 1 mm s^{-1}, but reproducibility of the averaged measurements was not discussed by Cooksey and Yang.[10] For example, the anode bases are horizontal, and it is known that slight inclinations can lead to significant changes in flow because it gives the bubbles a preferred direction. Sensitivity to tolerances could therefore be significant, in which case reproducibility of the flows (and hence the averaged measurements) could be an issue. As will be discussed below, comparison of measurements for different configurations suggest reproducibility is of order 10 mm s^{-1}.

In contrast to the center and side channels, strong recirculating flow (across the narrow dimension) is not predicted to form in the narrower (40 mm) duct-end channel. This is because the bubble plume diffuses across most of the channel width, so recirculation is weak and constrained to the bottom part of the channel. Although measurements were not made in the end

channels, observations confirm this model prediction. This change in flow pattern as channel width reduces is likely to be significant for heat transfer and ledge formation, since there will be a qualitative change in heat transfer characteristic at this point.

The inter-anode gaps are also too narrow for recirculation to occur (across the narrow dimension)—water is dragged upward to the surface where it then flows outward (in both directions) to the center and side channels. This is shown in the flow fields given in Figures 2(c) and (d), although the absence of measured flow at the surface into the side channel is curious—such flow was certainly observed at times in the water model during operation.

Figure 4 gives a comparison between measured and predicted velocity components on the plane through the middle of the inter-anode gap, where the plane crosses the side and center channels. The model plots at height 0.16 m show the outward flow of water from the inter-anode gap into side and center channels near the top surface of the bath. This jet reinforces the recirculation which exists along the entire length of the two channels, but also introduces some movement of water along the length of the channels away from the inter-anode gap.
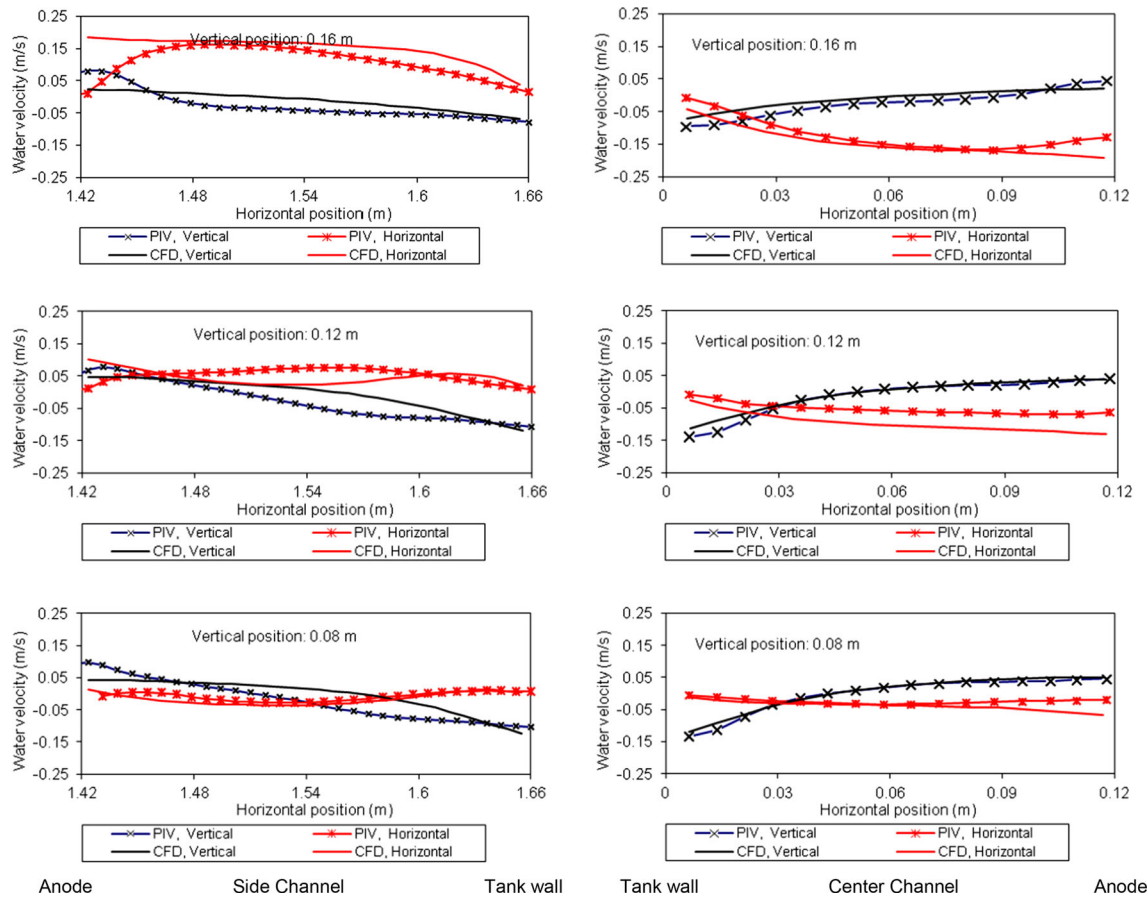
Fig. 4—Comparison for Configuration 1 between PIV measurement and CFD simulation of water velocity on inter-anode gap plane in side channel (location C) and center channel (location D) shown on left side and right side respectively.
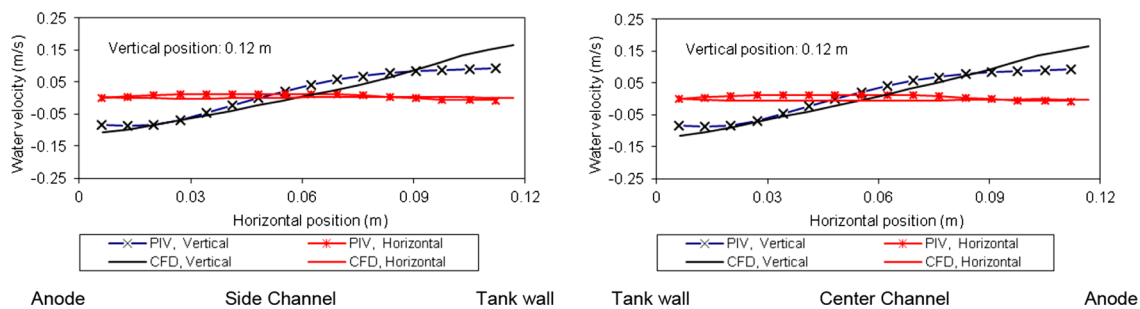

Fig. 5—Comparison between PIV measurement and CFD simulation of water velocity center channel at mid-anode in Configuration 1 (location B in Fig. 1): left, standard case CFD simulation; right, enhanced CFD model with bubble correction.

Agreement is generally good between measured and model velocities in the center channel, although, as mentioned above, outflow from the inter-anode gap into the side channel at the top surface of the water is over-predicted, as can be seen from Figure 2.

The velocities plotted in Figures 3 and 4 were obtained using the standard CFD model. The enhanced model gives very similar values, as demonstrated by the comparison given in Figure 5 for one traverse. The other traverses show similar behavior, and so are not given here.

B. Configuration 2: Case with 20 mm Inter-anode Gap Width and No Slot

To maximize the productivity of a cell, the gaps between anodes should be kept as narrow as possible. However, if the gaps are too narrow, they will choke off the flow of bubbles, presumably leading to a higher gas holdup under anodes and a higher bubble resistance. It is interesting, therefore, to investigate how the flow and gas distribution changes if the inter-anode gap width is halved from 40 to 20 mm. Measurements were reported

by Cooksey and Yang[10] for 20 mm gaps, and the CFD model has been run for this case.

Figure 6 gives measured and computed vector velocity plots of flow for all four positions in the side and center channels. Detailed point velocity comparisons along the three traverses through the channels are shown in Figure 7 (for the mid-anode plane) and Figure 8 (for the inter-anode gap plane). Comparison of Figures 2 through 4 with Figures 6 through 8 shows very little consistent difference between the measurements for the 40 and 20 mm gap cases; the only consistent variation is that the measured plume rise velocity is about 20 pct higher in the center channel for the 20 mm case, and slightly higher in the side channel. In the center channel at the inter-anode gap and height of 0.16 m, the measured vertical velocity in Configuration 2 is 0.20 m s^{-1}, compared with only 0.05 m s^{-1} in Configuration 1. This is a major difference that will be discussed further below.

As a result of the higher measured velocities, there is better agreement between the model and data velocities in the bubble plume for Configuration 2 than for the 40 mm gap case. Elsewhere however, the level of agreement between measured and computed flows is similar in the 20 mm case to the 40 mm case.

The reason for the higher measured bubble plume velocity in the center channel in Configuration 2 is not clear. If less gas escapes into the narrower inter-anode gap, then more gas will escape directly into side and center channels at the side of the anodes. However the side channel plume velocity is almost the same in the two configurations. Furthermore, the water velocity moving outward horizontally from the inter-anode gap at the top surface is significantly higher in Configuration 2 (particularly in the side channel), whereas the reverse would be expected if less gas escapes into the gap.

The CFD model predicts very similar velocities for Configurations 1 and 2 (40 and 20 mm inter-anode gap widths), with the latter slightly (up to 5 pct) higher. This fact, together with the difficulty of explaining the experimental differences in a consistent way, suggests that some of the larger differences found experimentally between the two configurations may be a reflection of reproducibility issues. Changing the inter-anode gap requires moving the anodes, so exact horizontal alignment for both cases is unlikely, yet the flows will be sensitive to small deviations in the anode base from the horizontal. Further measurements would be needed before the experimental differences can be considered significant.

When comparing the velocities for Configuration 1, the unusual lack of measured flow at the surface of the inter-anode gap into the side channel was pointed out. On the other hand, it can be seen from Figure 6 that for Configuration 2, there is much more surface flow out of the inter-anode gap at the side channel than there is at the center channel, just the reverse of Configuration 1. It is difficult to explain this difference on the basis of a smaller gap width: it is much more likely to be due to lack of reproducibility in the flows, understandable given the sensitivity of the flows to small geometrical tolerances.

C. Configuration 4: Case with 20 mm Inter-anode Gap Width with Slot

The measured and predicted flow and turbulence fields for configuration 4 (i.e., 20 mm inter-anode gap width with a slot through the middle anode) are compared in Figure 9. As for the other configurations, the flow pattern and turbulence distribution are well predicted. Figures 10 and 11 give point comparisons of vertical and horizontal velocities: again, as for the other configurations, the model velocities agree with the measurements within 10 mm s^{-1}, and in most cases significantly better.

As seen for the inter-anode gap in configurations 1 and 2, the measured flow exiting the slot appears to have a preferential flow direction, rather than an equal division between center and side channels, as predicted. In this case, the flow preferentially leaves the slot towards the center channel, though flow into the side channel is not entirely absent. This can be seen both in the vector plots (Figure 9) and the point comparisons (Figure 10): at position A at height 0.16 m, the horizontal outflow from the slot is zero, and the vertical velocity is significant (0.15 m s^{-1}). The same biased flow appears to occur in the inter-anode gap, with the center channel again preferred.

The measured turbulence in the surface flow exiting the slot is quite high, of order 100 pct turbulence intensity. This is higher than measured for the surface flow exiting the inter-anode gap in any configuration, and the cause of the high level of turbulence is difficult to understand, given that the flow would be expected to be similar to that in an inter-anode gap.

D. Configuration 3: Case with 40 mm Inter-anode Gap Width with Slot

The measured and predicted flow and turbulence fields for configuration 3 (i.e., 40 mm inter-anode gap width with a slot through the middle anode) are compared in Figure 12. As for the other configurations, the flow pattern and turbulence distribution are well predicted.

Unlike configuration 4, the measured surface flow from the slot appears to exit more or less equally into both center and side channels, as is the case for the predicted flow. Furthermore, these flows exiting the slot are not associated with the high level of measured turbulence found in configuration 3. These measured differences between configurations 3 and 4 cannot be easily explained as due to the change in the inter-anode gap width, and are more likely to be due to intrinsic sensitivity of the flow to slight changes or imperfections in the anode configuration set-up, or to medium-term variability in the flow field.

E. Flow Beneath the Anodes in the ACG

Cooksey and Yang[10] also measured the flow under the anode on the horizontal mid-plane of the ACG, i.e., half-way between the bottom of the anodes and the base of the tank. Figure 13 compares the measured and
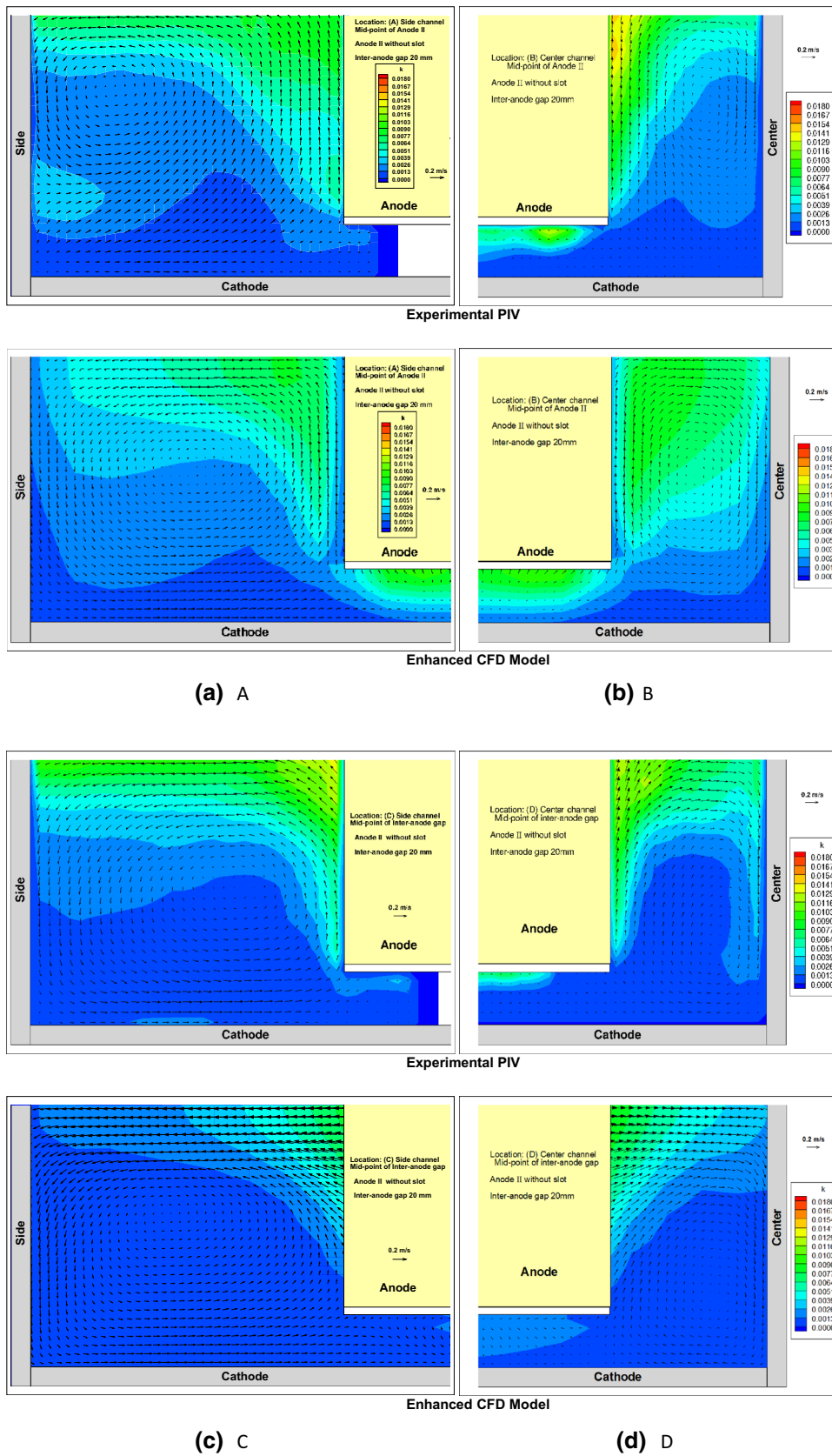
Fig. 6—Measured and predicted liquid velocity and turbulence for Configuration 2 (Anode II without slot, 20 mm inter-anode gap) at four locations: (*a*) A; (*b*) B; (*c*) C; (*d*) D. In each case, PIV measurements (top) are compared with CFD model with bubble correction (lower).
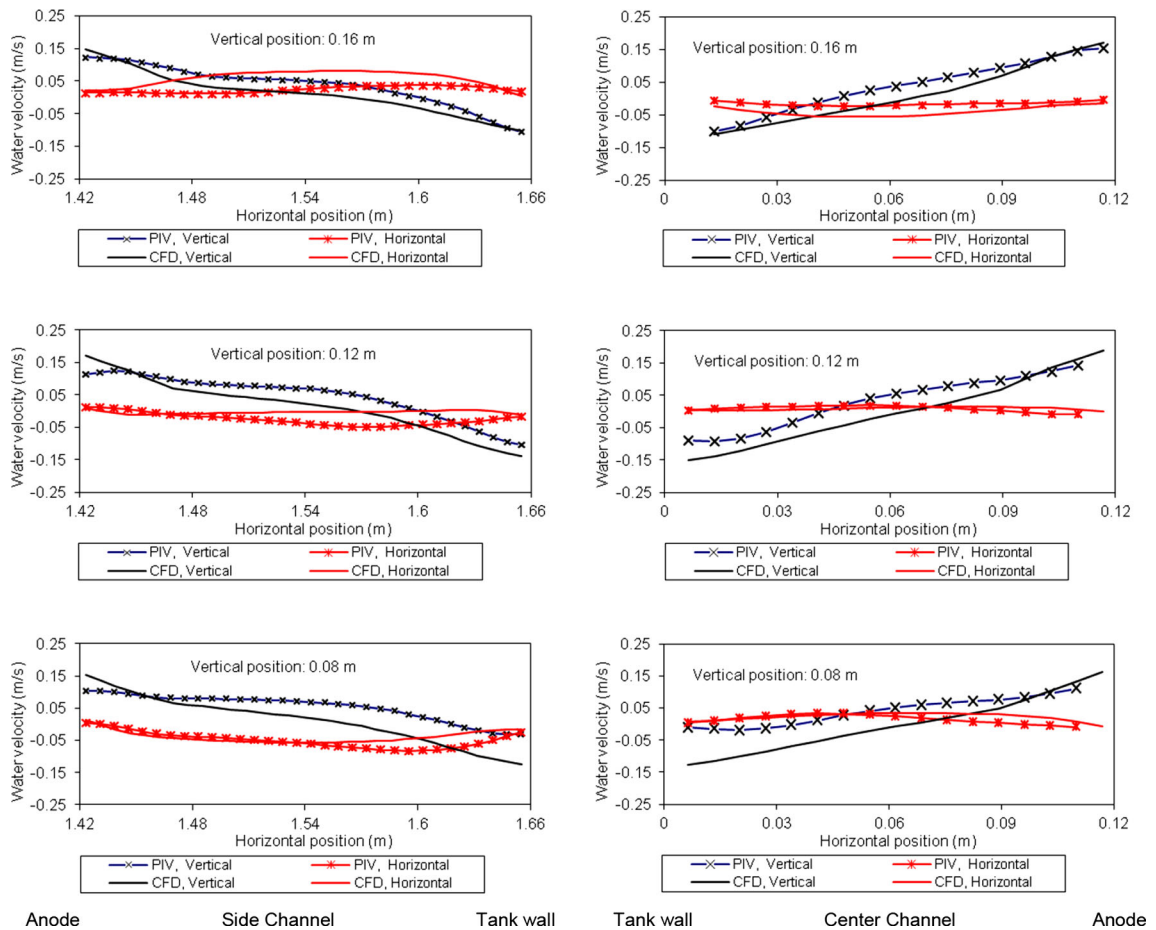
Fig. 7—Comparison for Configuration 2 between PIV measurement and CFD simulation of water velocity on mid-anode plane in side channel (location A) and center channel (location B) shown on left side and right side respectively.

predicted two-dimensional streamlines of the flow on this plane. Water is entrained into the ACG from the center, side and end channels, and dragged by bubbles up into the inter-anode gaps. Some water will also be dragged by bubbles sliding on the bottom faces of the anodes back into the side, center and end channels. The flow indicated in Figure 13 is surprisingly complex, and the agreement between the prediction and the measured fields is remarkably good, given the likely sensitivity of flow in the ACG to any minor imperfections in the flatness of the anodes. As an example, air is injected into the ACG through many separate compartments in order to ensure uniform flow rate across the anode bottoms. This results in joins between Perspex blocks which will inevitably have some effect on bubble movement despite extreme care taken in construction. Furthermore, no gas injection occurs at walls between compartments, and this non-uniformity in gas generation was not accounted for in the CFD model.

This plane indicates the return flow at the bottom of the various channels surrounding the anodes. In the side and tap-end channels, this flow is quite strong, up to 0.12 m s^{-1} in both predicted and measured flow fields, whereas this return flow in the center and end channels is only about half this velocity. This disparity is a result of the difference in the channel width. As previously

noted, the narrow duct-end channel does not allow a vertical recirculation to develop fully—the bubble plume spreads across most of the channel width, thereby impeding the downward return flow. For this reason, recirculation is constrained to the lower part of the channel and is weaker than in the tap-end channel. Figure 13 indicates that this is the case both for the numerical model and the physical model, and this is strong confirmation of the CFD model, including aspects such as the extent of turbulent bubble diffusion. Note that this conclusion can be drawn even though measurements of velocity were not made in the tap-end channel.

It is important to emphasize that the tap-end and duct-end channels are distinguished in the present physical model solely by their width. The conclusion concerning the different recirculation strengths would only apply to real tap-end and duct-end channels if their widths were similar to those in the physical model studied.

It is worthwhile to point out the salient features of the flow field beneath the anodes, which in all cases are seen in both predicted and measured flows. First, the flow fields beneath the anodes are all different. It is expected (and this has been found from modeling[21,36]) that when there are more than three anodes along the length of the
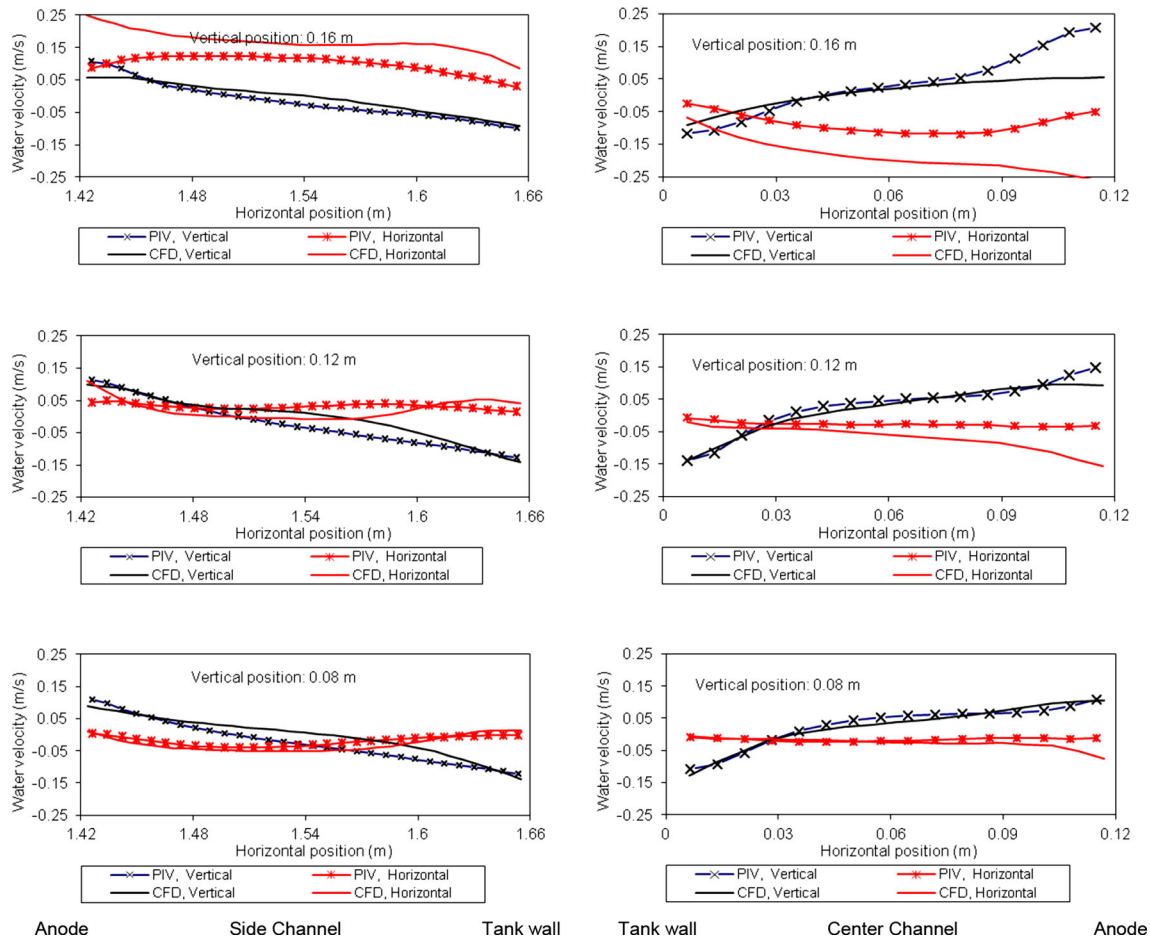
Fig. 8—Comparison for Configuration 2 between PIV measurement and CFD simulation of water velocity on inter-anode gap plane in side channel (location C) and center channel (location D) shown on left side and right side respectively.

cell, the flows associated with each internal anode are very similar. It is not surprising that the flows at the end anodes are different from internal anodes. In the present case, the flows associated with the two end anodes are different, and this is entirely due to the different channel widths assumed—no other significance should be ascribed to the difference. Indeed, the difference in the flows associated with the two end anodes is remarkable—not just in quantitative terms but also in terms of the topology of the flow. At the tap-end, there is entrainment of electrolyte from the end channel into the ACG. On the other hand, at the duct end, electrolyte is expelled from the ACG into the end channel. This is perhaps due to the much weaker vertical recirculation in the duct-end channel, which has been described above. As previously mentioned, the weaker recirculation is due to the narrow duct-end channel.

The side and center channels are more consistent in terms of the direction of electrolyte movement into or out of the ACG. In both cases, electrolyte is entrained into the ACG on the mid-plane, except for small regions at the tap end of each channel where electrolyte is expelled.

Noticeable features are the vortices that occur near the corner of the anode at intersection of center and tap-end channels, and to a lesser extent the corners at side

and tap-end channels and at the intersection of one of the inter-anode gaps and the center channel. These vortices are seen in both predicted and measured fields with similar relative strengths. Since flow converges at the vortex centers, electrolyte must then be entrained upward in a rather stronger flow at these points. Although the rounded edges of worn anodes may reduce the intensity of such vortices, it is likely they exist in real cells, and must have an influence on mixing.

The convergence of streamlines onto two lines aligned beneath and along the inter-anode gaps is indicative of the flow converging on these lines and then being entrained up into the gaps. Although there are no bubbles present on the mid-plane of the ACG (the plane plotted), the bubbles sliding on the lower face of the anodes and then rising into the gaps under the effect of buoyancy creates a negative pressure that results in the entrainment of electrolyte from the rest of the ACG.

The predicted flow fields on the mid-plane of the ACG have been compared for the four configurations, with Figure 14 showing the resultant flow for Configurations 1 and 3. It is found that halving the inter-anode gap width from 40 to 20 mm makes almost no difference to the flow field. On the other hand, the installation of a slot changes the flow field under the middle anode. As expected, the entrainment of elec-
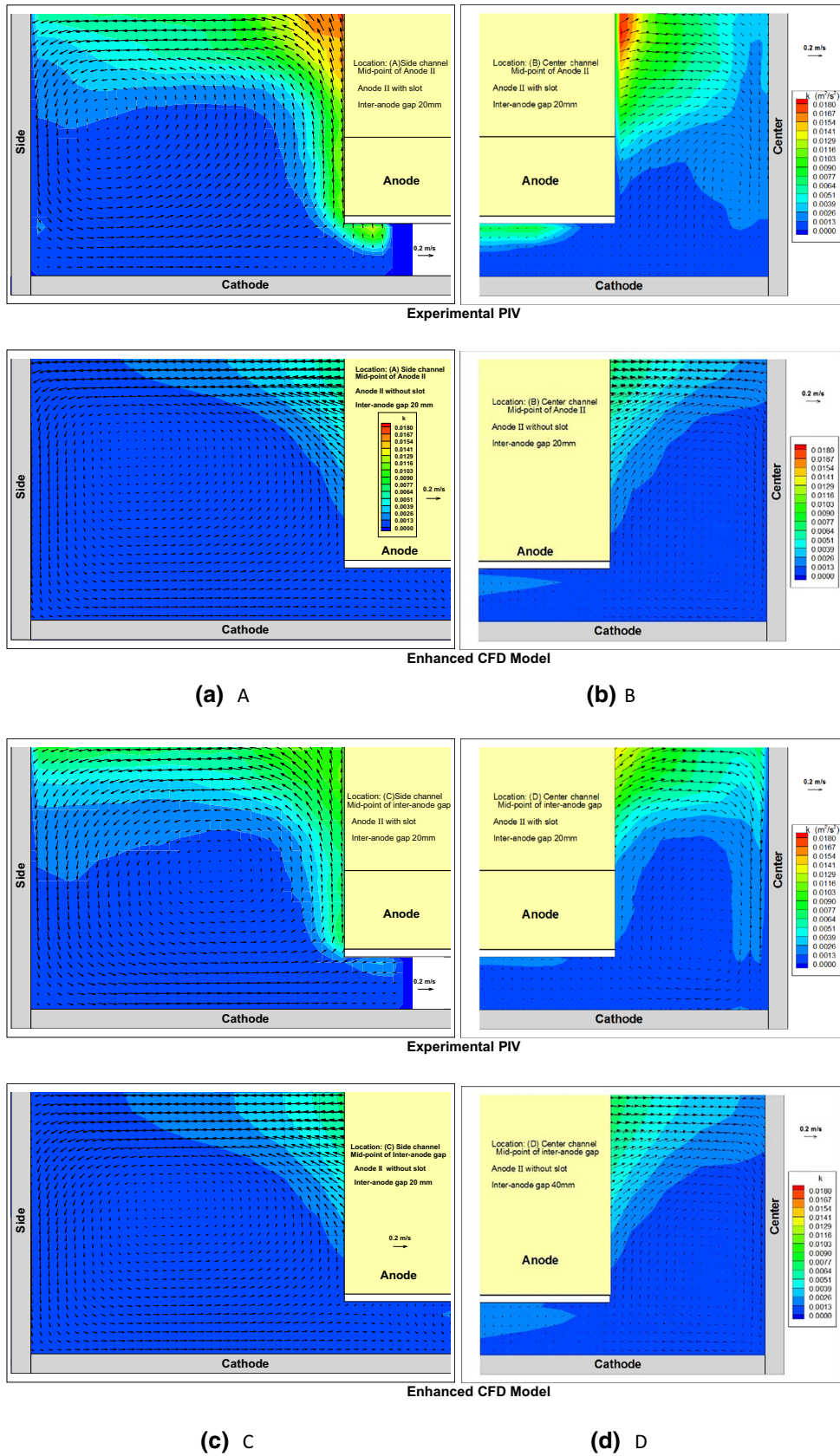
Fig. 9—Measured and predicted liquid velocity and turbulence for configuration 4 (Anode II with slot, 20 mm inter-anode gap) at four locations: (*a*) A; (*b*) B; (*c*) C; (*d*) D. In each case, PIV measurements (top) are compared with CFD model with bubble correction (lower).
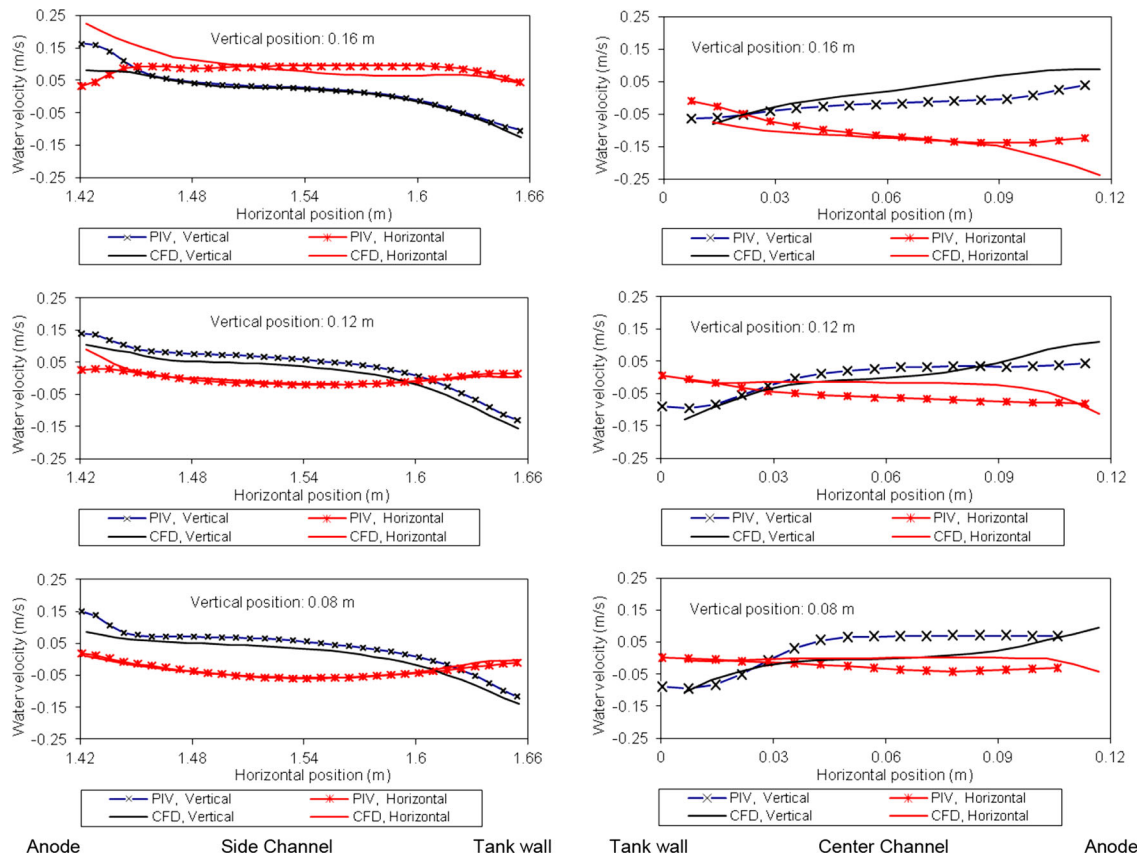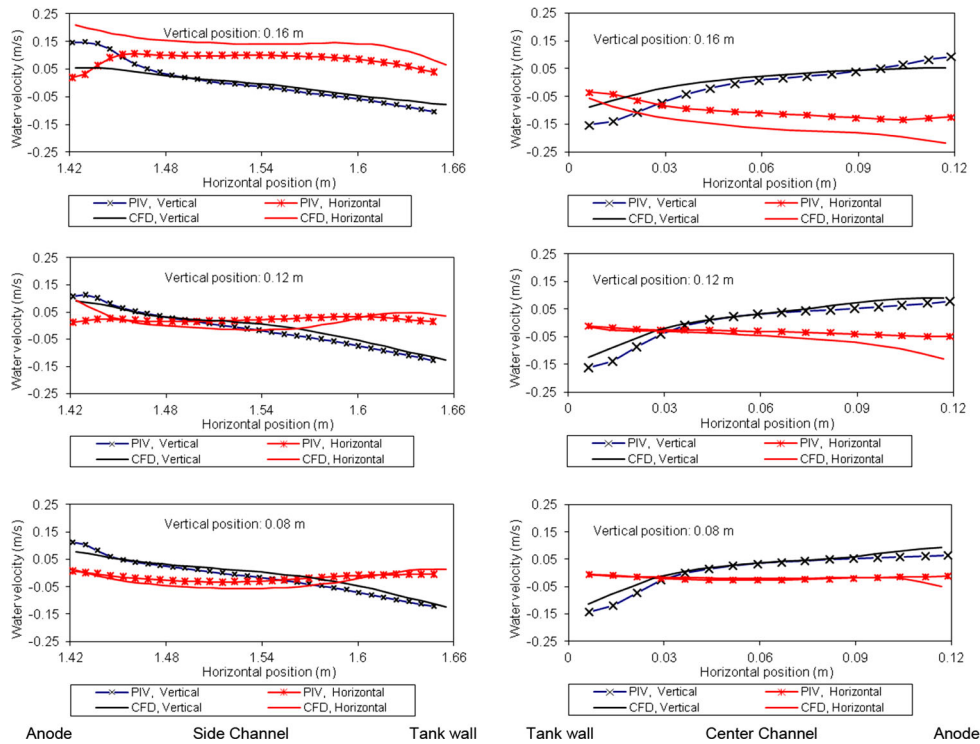
Fig. 10—Comparison for Configuration 4 between PIV measurement and CFD simulation of water velocity on mid-anode plane in side channel (location A) and center channel (location B) shown on left side and right side respectively.
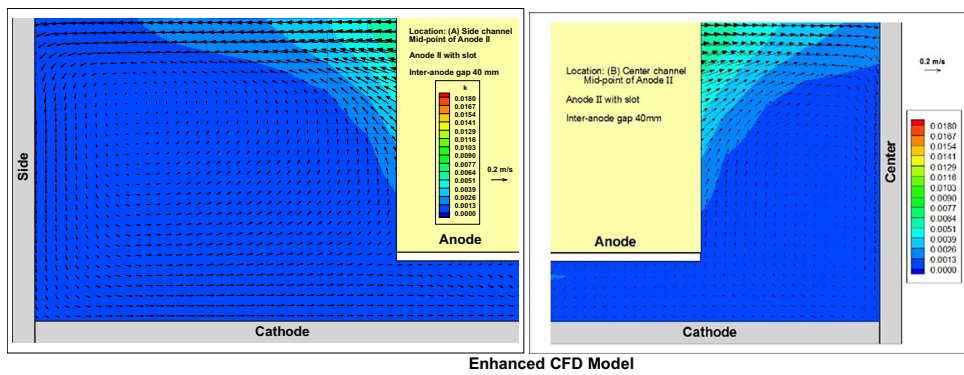

Fig. 11—Comparison for Configuration 4 between PIV measurement and CFD simulation of water velocity on inter-anode gap plane in side channel (location C) and center channel (location D) shown on left side and right side respectively.
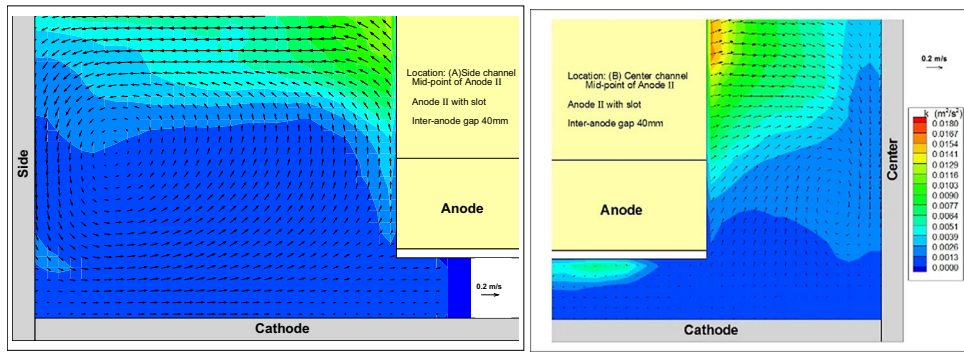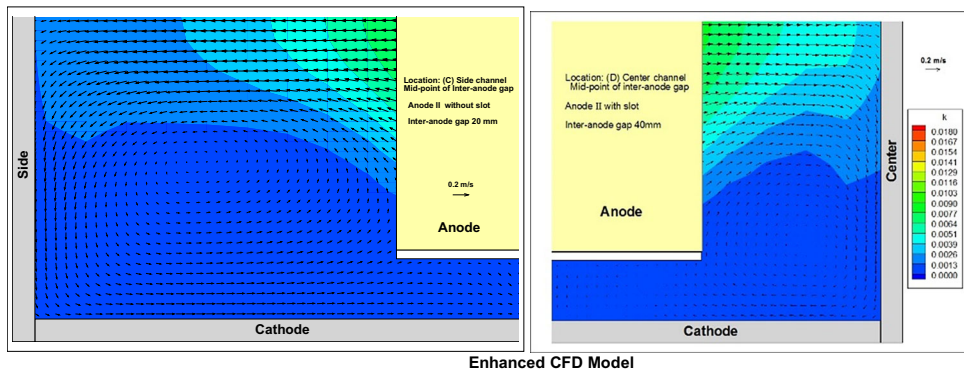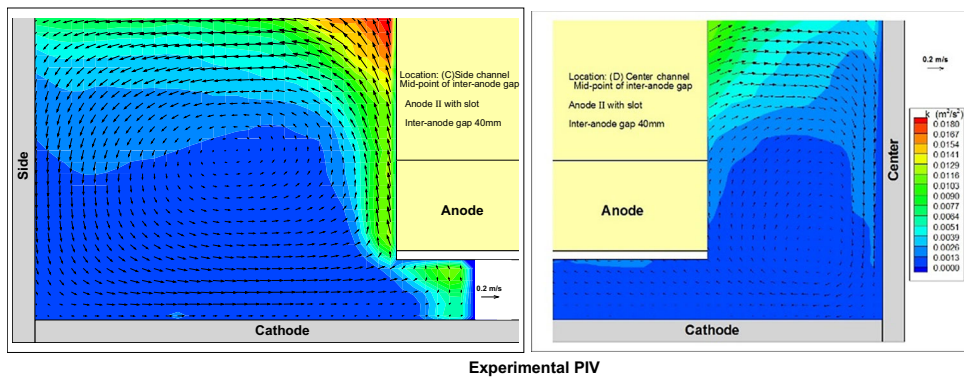
Fig. 12—Measured and predicted liquid velocity and turbulence for configuration 3 (Anode II with slot, 40 mm inter-anode gap) at four locations: (*a*) A; (*b*) B; (*c*) C; (*d*) D. In each case, PIV measurements (top) are compared with CFD model with bubble correction (lower).
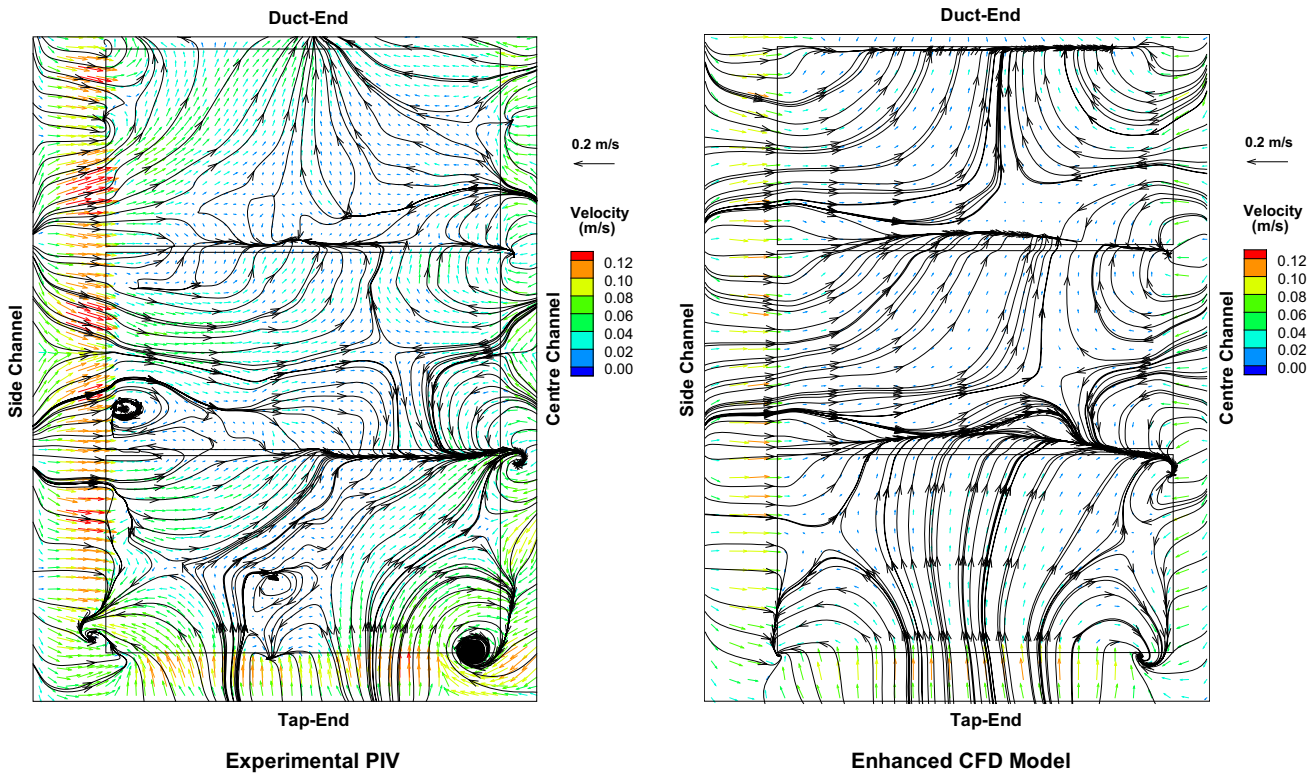
Fig. 13—Measured (left) and predicted (right) liquid velocity and streamlines for configuration 2 (Anode II without slot, 20 mm inter-anode gap) on a horizontal plane through the middle of the ACG.
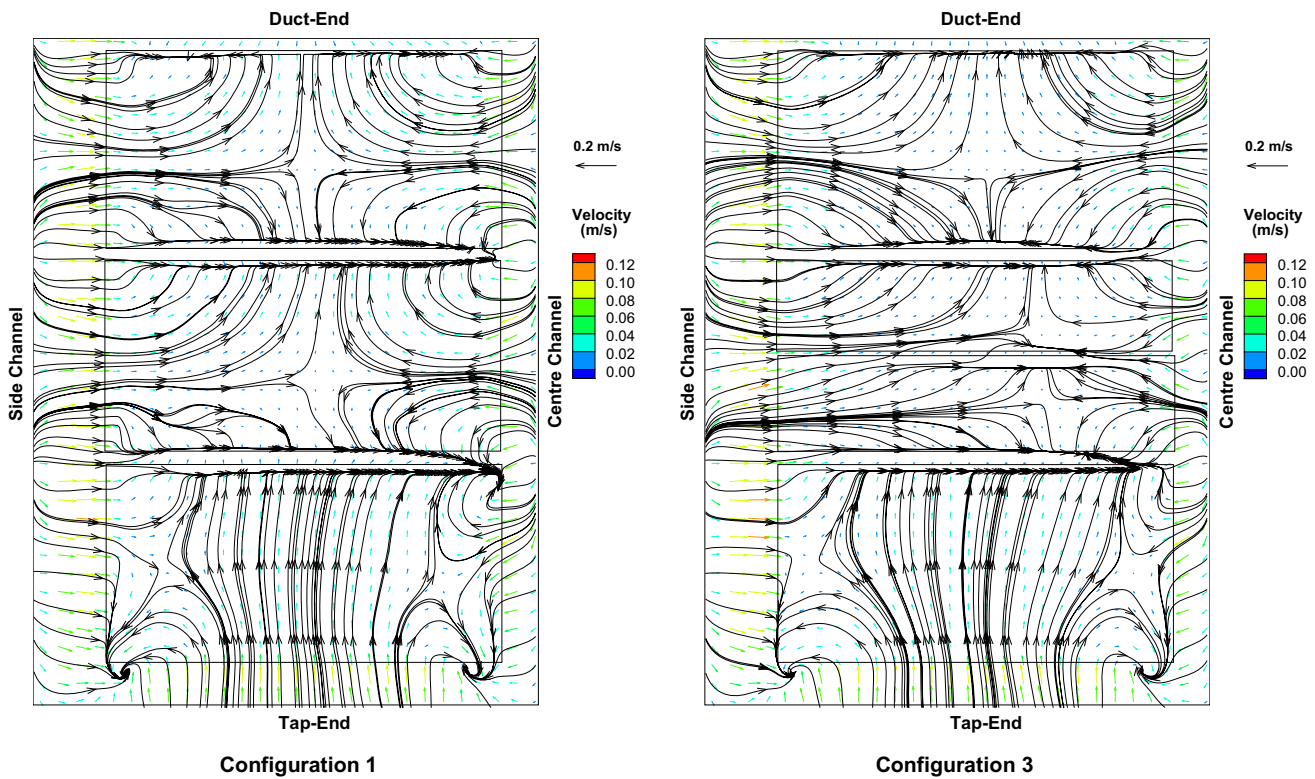

Fig. 14—Predicted liquid velocity and streamlines for configuration 1 (Anode II without slot, 40 mm inter-anode gap) and configuration 3 (Anode II with slot, 40 mm inter-anode gap) on a horizontal plane through the middle of the ACG.

trolyte into the slot as well as the gaps results in convergence of streamlines on the mid-plane onto three lineal zones—under the two gaps and the slot.

VI. COMPARISON BETWEEN CONFIGURATIONS

The predicted flow fields on the measurement planes are all qualitatively similar, reflecting the recirculation generated in the center and side channels by rising gas bubbles. The major difference is that introduced by the addition of a slot across the middle anode. This results in a modification of the flow on the plane bisecting the middle anode—rather than the strong upward flow in the plume beside the anode found without the slot, there is a strong, almost horizontal, flow out of the slot, particularly near the surface.

The predicted flows on the measurement planes are almost identical for the two inter-anode gap cases, and this is true for both configurations with and without slot. This is not surprising given that it is expected that the same amount of gas would end up releasing through the gap whether it is 20 or 40 mm.

On the other hand, there are some apparent differences between the measured flow and turbulence fields of the various configurations. One of the most noticeable variations is in the flow near the gap or slot, particularly near the surface. In some cases, there is much more flow exiting the gap (or slot) into the center channel with very little flow from the gap (or slot) into the side channel. Sometimes this situation is reversed, with a preferential flow from the gap (or slot) into the side channel; and thirdly, sometimes the flows are split more evenly into the two channels. There appears to be no pattern controlling which situation applies in any particular configuration. This suggests that the variations are likely to be due to non-repeatability of the flow. There are two possible causes for this behavior that can be identified.

Firstly, the bottom faces of the anodes are horizontal. Any slight deviation from exact horizontal alignment would lead to a significant directional bias in the flow of buoyancy-driven bubbles under the anodes. Since the anodes must be moved to adjust the gap, it is possible that the alignment is changed slightly for each configuration.

Secondly, bubbly flows such as the one studied here are known to be subject to medium time-scale internally-generated variability. This is true of large bubble columns and bubble plumes in large systems,[37] where the meandering behavior (which can be random or quasi-periodic) can have a time-frame of 30 to 60 seconds, or even longer for very large systems. The feedback time in the aluminum cell water model is likely to be at least of a similar order given the feedback path lengths of order 1 m, and the low water velocity (of order 10 mm s^{-1}) over most of the feedback path. If such variability occurs, averaging over 20 minutes or more could be required to obtain a long-term average.

Such variability would have process implications for aluminum cells, and in particular implications for cell control. It is well known that cell operation is variable on a wide range of different time-scales, though most of the variability on this time-scale can be explained in terms of waves on the metal pad.

Comparison of the measured turbulence energy distributions for the four configurations is similarly inconclusive. It would be expected that the increase in inter-anode gap width from 20 to 40 mm would have a similar effect at the inter-anode gap plane in both center and side channels since the turbulence there is dominated by the flow exiting the gap. Also, this would be expected to be the case for both configurations with and without slot. For the configuration without slot, the turbulence energy level slightly decreases in both channels at the surface as the gap width is increased. This is consistent with the slightly lower velocities measured. On the other hand, for the configuration with slot, the turbulence energy increases substantially in the side channel (the maximum value doubles), while decreasing significantly in the center channel (the maximum value by 35 pct) as the gap width is increased. This apparent inconsistency supports the conclusion above that the flow configurations measured had some limitations with regard to reproducibility.

The turbulence level on planes A and B is generally measured to be higher for slotted cases (in which case these planes align with the slot) than for cases without slot. For example, for 20 mm inter-anode gap, the slotted case (Figures 9(a) and (b)) shows a higher measured turbulence level than the case without slot (Figures 6(a) and (b)). This trend is not reproduced in the CFD model results, where the turbulence is lower in case of the slotted anode, partly because of the absence of bubbles releasing from the bottom of the anode, and the consequent absence of a bubble plume. The measured trend is however not consistent. For the 40 mm inter-anode gap, the measured turbulence level is lower in the case with a slot (Figure 12(a)) than the case without the slot (Figure 2(a)): the measured turbulence level is about the same in the upper half of the plot, but lower in the bottom half, presumably because of the absence of plume gas, as in the model results. Despite this lack of complete consistency in the experimental trends, taken as a whole, the data suggest higher turbulence on the plane through the slot. One factor affecting the model prediction of turbulence level on this plane would be the assumption of a flat top bath surface. The stream of water from the slot could well be subject to waves and side-to-side oscillation which may increase the turbulence level. This aspect of the model needs further work.

Of course, the reason for studying the effect of a slot is that such a modification should result in faster release of bubbles from under anodes, with the resultant reduction in bubble holdup and consequently lower bubble voltage. It is therefore of interest to investigate the effect of the slot in Configurations 3 and 4 on holdup beneath the anodes. The holdup is calculated by integrating gas volume under the middle anode, and expressing the value as volume of gas per square meter of anode bottom area. For configurations 1 and 2, the holdup is almost identical at 0.0042 m^3 m^{-2}, while for configura-
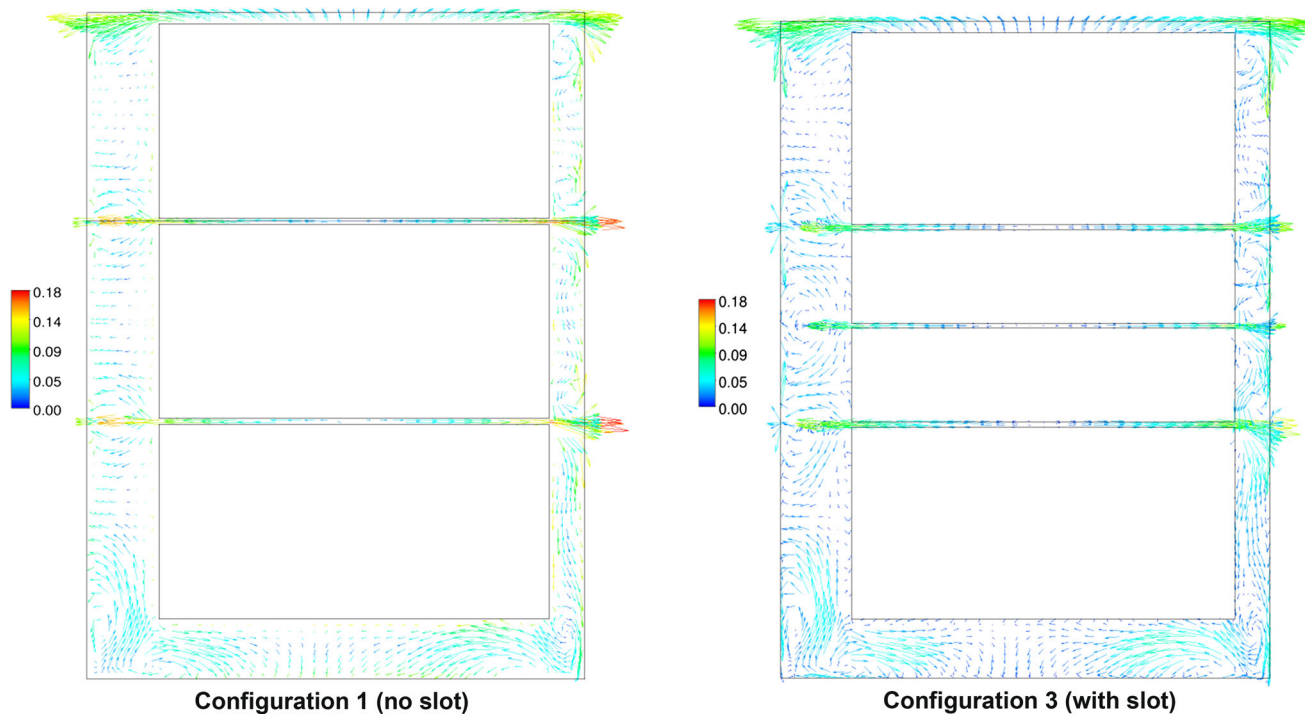
Fig. 15—Comparison of predicted liquid velocity vectors for Configurations 1 (left, no slot) and 3 (right, with slot) on a horizontal plane through the middle of the anode. Color scale shown in m s^{-1} (Color figure online).

tions 3 and 4, the holdup is 0.0021 m^3 m^{-2}. It is not surprising that the holdup is halved by the presence of the slot, since the travel distance of most bubbles before release is halved. This result agrees with the work carried out by Feng et al.,[19] for an earlier version of the model.

It is instructive to also consider the effect of the slot on cell mixing. Figure 15 compares predicted liquid velocity vectors for Configuration 1 (without slot) and Configuration 3 (with slot) on a horizontal plane half-way up the anode. The longitudinal mixing in the side channel in the absence of the slot is rather poor. In fact, streamlines in this channel move only slowly along the length of the cell. While turbulent diffusion will increase this mixing, it is generally less effective than mean flow convective mixing. Longitudinal mixing in the center channel is more effective, with streamlines executing faster helical motion along the channel. It appears that bubbles pump more electrolyte into this channel than is re-entrained back into the ACG, resulting in a mean flow from the middle of the center channel towards the end channels. On the other hand, it appears that bubbles pump less liquid into the side channel compared with the amount entrained into the ACG, with the result that there is no such mean flow towards the end channels. This difference is presumably due entirely to the difference in channel widths.

The addition of the slot in Configuration 3 increases the degree of longitudinal motion in the side channel: the jet exiting the slot creates two additional recirculations that will undoubtedly increase longitudinal mixing. These recirculatory patterns will also break down to generate more turbulence, and hence improve the turbulent diffusion component of mixing.

It is also worth noting in Figure 15 that the flow is quite intense in the duct-end channel. Recall that liquid is expelled from the ACG into the duct-end channel on the mid-plane (rather than the reverse, as occurs in almost all other regions). This means that there must be a net flow away from the middle of the duct-end channel towards the side and center channels, as seen in Figure 15. It can be seen therefore that the relative widths of the center, side, and end channels have a major influence on several critical aspects of the cell flow field.

Figure 16 compares predicted void fraction color contours for Configuration 1 (without slot) and Configuration 3 (with slot) on a horizontal plane half-way up the anode. As mentioned above, bubbles extend across most of the width of the duct-end channel in both configurations, whereas the bubble plume occupies only a minor fraction of the tap-end channel width. This results in suppression of vertical recirculation in the duct-end channel compared with the tap-end channel. The addition of the slot reduces the bubble voidage in the inter-anode gaps and also the number of bubbles rising next to the middle anode in the center and side channels.

VII. DISCUSSION

Comparison between experimental measurements of velocity and turbulence and model results described in the previous sections indicate a reasonable degree of agreement. One significant issue of difference between the model and data relates to the prediction of the
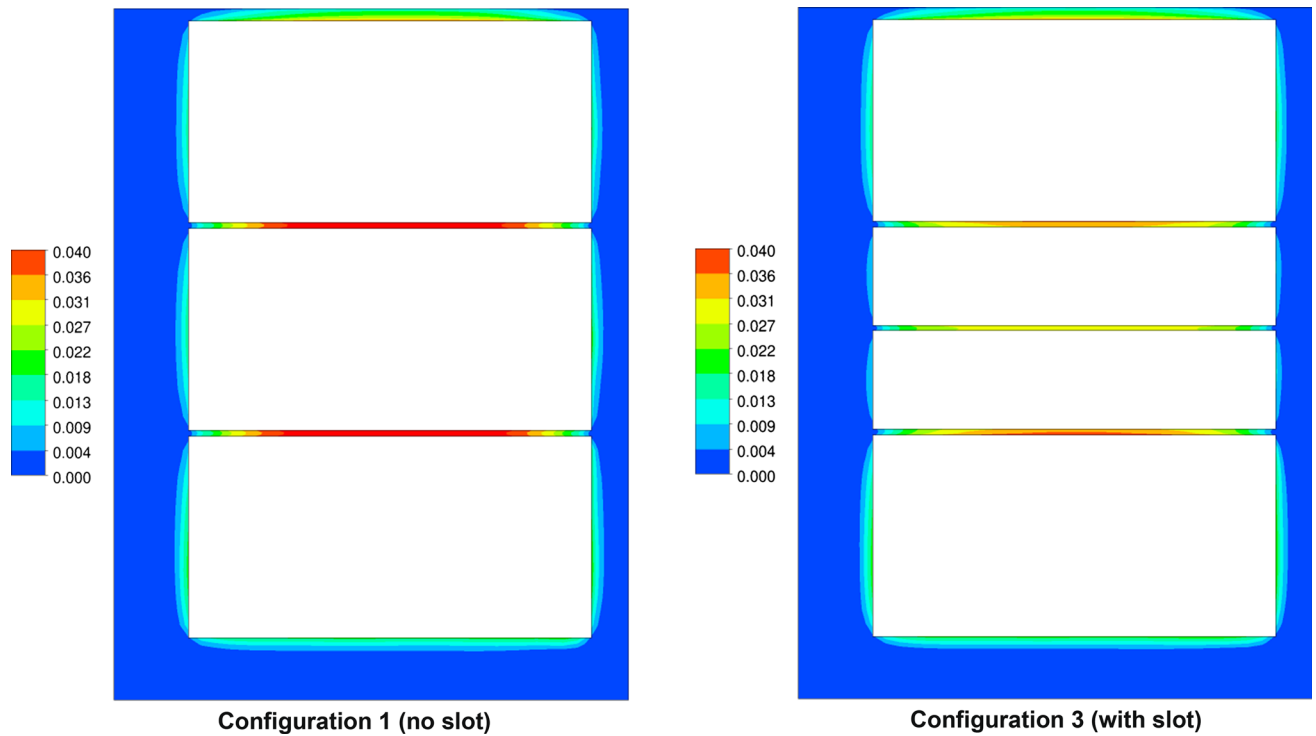
Fig. 16—Comparison of predicted bubble voidage for Configurations 1 (no slot) and 3 (with slot) on a horizontal plane through the middle of the anode. Color scale shown as void fraction (Color figure online).

surface flow exiting the gaps (and the slot for configurations 3 and 4). The model predicts a more or less equal distribution of flow exiting into the center and side channels, where the measured data indicate that the flow is in some cases biased to the center channel, in some cases to the side channel, and in some cases the flow is more or less equally split. It is not possible to relate the measured outcome to the configuration in any plausible way, so it seems likely that this aspect of the flow may be non-reproducible. This could be due either to long time-scale variability of the flow, or to the sensitivity of the average flow to slight deviations in the degree to which the bottom of the anodes is aligned horizontally. With regard to the first of these possibilities, it is well known that laboratory scale bubble columns are subject to variability on a time-scale of order at least 1 minute.[37] If such variability occurs in industrial cell hydrodynamics, there would be significant process implications. It is well known that cell operation is subject to variability on a wide range of time-scales, and it is entirely plausible that some of that variability could be due to such hydrodynamic instability.

The measured level of turbulence in the surface flows exiting the gap and slot also vary by up to a factor of two in a way which is not possible to explain in a consistent fashion based on configuration. It is possible that this variation is also a reflection on non-repeatability of the flow. The predicted turbulence level in these streams is more consistent with the flow field changes, and shows less variation between configurations.

Overall, the predicted flows on the measurement planes does not depend to a great extent of the

configuration, with the exception that, with the presence of the slot, there is a surface stream exiting the slot into the channels. Indeed, there is more variation from one configuration to another in the experimental measurements than in the model results, though as mentioned above, it is often difficult to understand how the variations in the mean velocity could result from the relatively minor configuration changes.

Detailed examination and analysis of the computed flow fields leads to the conclusion that the relative widths of the center, side, and end channels have a major influence on several critical aspects of the cell flow field. This is seen most clearly by examining flows on horizontal cross sections. For example, the flow field on the mid-plane of the ACG (Figures 13 and 14) indicates that the flow beneath the two end anodes is quite different, both quantitatively and in terms of topology. While liquid is entrained from the tap-end channel into the ACG, liquid is expelled from the ACG into the duct-end channel. This can only be due to the narrower width of the duct-end channel. Longitudinal mixing in the wide side channel is found to be lower than in the (narrower) center channel, though addition of a slot is found to improve the mixing. Similarly, the model predicts a vigorous movement out of the narrow duct-end channel to the center and side channels, in a way not found in the (wider) tap-end channel.

An additional finding related to channel width is that while strong recirculating flow (across the narrow dimension) occurs in the wide center and side channels, it is not predicted to form in the narrower (40 mm) duct-end channel. This is because the bubble plume diffuses

across most of the channel width, so recirculation is weak and constrained to the bottom part of the channel. This change in flow pattern as channel width reduces is likely to be significant for heat transfer and ledge formation, since there will be a qualitative change in heat transfer characteristic at this point. There will also be a qualitative change to mixing characteristic at the transition channel width. Of course in practice, end channel width is determined in part by the flow conditions themselves, since ledge formation is controlled in part by heat transfer, which itself is coupled to flow. It is expected that the heat transfer coefficient for bubbly upward flow in a narrow channel would be higher than in the more quiescent downward flow of a recirculation, so it might be expected that a ledge would melt until it is sufficiently wide for recirculation to occur, in the absence of other controlling factors. On the other hand, if a ledge were able to grow to such an extent that it choked off bubbly flow into a channel, the heat transfer coefficient could be reduced to a value that would stabilize the ledge.

As an example of the practical utility of the CFD model, the gas holdup under the anodes has been calculated for each configuration. The gas holdup does not change when the inter-anode gap width is increased from 20 to 40 mm. On the other hand, the presence of the slot results in a halving of the bubble holdup under the middle anode. This is an important result, because lower bubble holdup should translate to a lower bubble voltage, and hence lower energy consumption of the cell. The CFD model also predicts that mixing in the widest channel (in this case the side channel) is enhanced by the addition of a slot. Of course, the situation is more complex for an industrial cell: slots will be consumed as an anode is consumed, so the arrangement of slots in the cell will change as various anodes are replaced. These issues need to be studied in greater detail in order to design an optimum slot arrangement, and the CFD model described in this paper provides a useful tool to carry out this design process.

VIII. CONCLUSIONS

A two-phase CFD model has been developed to simulate the flow in the molten electrolyte layer of a Hall–Héroult aluminum cell. The flow is driven by the rise of carbon dioxide bubbles formed on the base of the anodes, and is a complex turbulent flow with interaction between multiple recirculating regions in the various channels formed by the anode configuration. The model has been developed based on the two-fluid formulation, in which Navier–Stokes equations are solved for each phase (bubbles and water) with interaction terms between the two fields. The approach is a time-averaged one, which seeks to determine the average flow field and bubble distribution, while accounting for the turbulent fluctuations by solving for differential field equations for turbulence energy (k) and the dissipation rate of turbulence energy (ε). The dispersion of bubbles by turbulence eddies, and the generation of additional turbulence by the movement of bubbles has been accounted for using specific additional terms in the equations. This is the first time use of these particular terms has been reported in the prediction of aluminum cell bath flow. Furthermore, the model has been enhanced to account for the finite size of bubbles in the plume relative to the computational grid dimension, an issue that is not normally encountered in two-fluid simulations.

The CFD model has been validated against detailed measurements of velocity and turbulence taken in a full-scale air–water physical model containing three anodes in four different configurations. The measurement planes on which comparison was undertaken are vertical planes bisecting the middle anode and bisecting one of the inter-anode gaps. The measurements were taken in both the center and side channels. The model predictions agree with the point velocity measurements and turbulence energy within the likely uncertainty of the measurements caused by difficulties in experimental reproducibility.

It was found that the relative widths of the center, side, and end channels have a major influence on several critical aspects of the cell flow field, particularly in relation to the entrainment from the channels to the ACG. Channel width is also found to affect whether vertically-aligned recirculation occurs in the channel, a finding that could be important for ledge heat transfer.

Decrease of the inter-anode gap width from 40 to 20 mm was found to have little effect on the flow field or the gas holdup under the anodes. On the other hand, the presence of the slot results in a halving of the bubble holdup under the middle anode, although the flows and holdup associated with the other anodes is unaffected. Lower bubble holdup should translate to a lower bubble voltage, and hence lower energy consumption of the cell. The CFD model also predicts that mixing in the widest channel (in this case the side channel) is enhanced by the addition of a slot. Overall, the predicted flows on the measurement planes does not depend to a great extent on the configuration, with the exception that, with the presence of the slot, there is a surface stream exiting the slot into the channels.

Given that the model has been validated using data on the measurement planes, it is then possible to study other aspects of the two-phase hydrodynamics using the model. Understanding the overall electrolyte circulation patterns and mixing can potentially be used to improve cell design and operation.

Further experimental and numerical work is needed to allow the model to be extended to incorporate a range of additional complex phenomena, including bubble size and shape effects under the anode and in inter-anode channels; rapid and longer-term transient behaviors; the effect of a deformable free surface at the top of the electrolyte; and the effect of a deformable metal-bath interface.

REFERENCES

1. K. Grjotheim and B.J. Welch: *Aluminium Smelter Technology*, 2nd ed., Aluminium-Verlag, Dusseldorf, 1988.
2. M.P. Taylor, R. Etzion, P. Lavoie, and J. Tang: *Metall. Mater. Trans. E*, 2014, vol. 1E, pp. 1–11.
3. A.V. Nikitin, V.A. Kryukovskii, and N.S. Mikhalitsin: *Sov. J. Non-Ferrous Met.*, 1975, vol. 16, pp. 37–40.
4. O. Kobbeltvedt and B.P. Moxnes: *Light Metals*, TMS, Warrendale, 1997, pp. 369–76.
5. E. Dernedde and E.L. Cambridge: *Light Metals*, AIME, New York, 1975, pp. 111–23.
6. A. Solheim, S.T. Johansen, S. Rolseth, and J. Thonstad: *J. Appl. Electrochem.*, 1989, vol. 19, pp. 703–12.
7. D.C. Chesonis and A.F. LaCamera: *Light Metals*, TMS, Warrendale, 1990, pp. 211–20.
8. R. Shekhar and J.W. Evans: *Metall. Mater. Trans. B*, 1994, vol. 25B, pp. 333–40.
9. J.J.J. Chen, X. Shen, M.P. Taylor, and B.J. Welch: *Light Metals*, TMS, Warrendale, 1996, pp. 343–50.
10. M.A. Cooksey and W. Yang: *Light Metals*, TMS, Warrendale, 2006, pp. 359–65.
11. S. Fortin, M. Gerhardt, and A.J. Gesing: *Light Metals*, TMS, New York, 1984, pp. 721–41.
12. J.M. Purdie, M. Bilek, M.P. Taylor, W.D. Zhang, B.J. Welch, and J.J.J. Chen: *Light Metals*, TMS, Warrendale, 1993, pp. 355–60.
13. A. Perron, L.I. Kiss, and S. Poncsak: *Int. J. Multiph. Flow*, 2006, vol. 32, pp. 606–22.
14. M. Alam, W. Yang, K. Mohanarangam, G. Brooks Y. Morsi: *Metall. Mater. Trans. B*, 2013, vol. 44B, pp. 1155–65.
15. S.T. Johansen: Ph.D. Thesis, University of Trondheim, Trondheim, Norway, 1990.
16. M.M. Bilek, W.D. Zhang, and F.J. Stevens: *Light Metals*, TMS, Warrendale, 1994, pp. 323–31.
17. M.A. Doheim, A.M. El-Kersh, and M.M. Ali: *Metall. Mater. Trans. B*, 2007, vol. 38B, pp. 113–19.
18. Y.Q. Feng, W. Yang, M.A. Cooksey, and M.P. Schwarz: *5th Inter. Conf. on Comput. Fluid Dynamics in the Process Industries*, Melbourne, Australia, 2006.
19. Y.Q. Feng, M.A. Cooksey, and M.P. Schwarz: *Light Metals*, TMS, Orlando, FL, 2007, pp. 339–44.
20. Y.Q. Feng, W. Yang, M.A. Cooksey, and M.P. Schwarz: *J. Comput. Multiph. Flows*, 2010, vol. 2, pp. 179–88.
21. Y.Q. Feng, M.A. Cooksey, and M.P. Schwarz: *Light Metals*, TMS, Warrendale, 2010, pp. 455–60.
22. J. Li, Y. Xu, H. Zhang, and Y. Lai: *Int. J Multiph. Flow*, 2011, vol. 37, pp. 46–54.
23. D.A. Drew and R.T. Lahey: *Int. J. Multiph. Flow*, 1979, vol. 5, pp. 243–64.
24. M.P. Schwarz and W.J. Turner: *Appl. Math. Model.*, 1988, vol. 12, pp. 273–79.
25. ANSYS CFX 15 User Manual, ANSYS Inc., 2013.
26. Y. Sato and K. Sekoguchi: *Int. J. Multiph. Flow*, 1975, vol. 2, pp. 79–95.
27. A. Sokolichin, G. Eigenberger, and A. Lapin: *AIChE J.*, 2004, vol. 50, pp. 24–44.
28. I. Kataoka and A. Serizawa: *Int. J Multiph. Flow*, 1989, vol. 15, pp. 843–55.
29. A.D. Burns, T. Frank, I. Hamill, and J.-M. Shi: *5th Inter. Conf. on Multiphase Flow, ICMF'04*, Yokohama, Japan, 2004, Paper No. 392.
30. J.F. Moraga, A.E. Larreleguy, D.A. Drew, and R.T. Lahey: *Int. J. Multiph. Flow*, 2003, vol. 29, pp. 655–73.
31. M. Sevik and S.H. Park: *J. Fluids Eng.*, 1973, vol. 95, pp. 53–60.
32. L. Schiller and Z. Naumann: *Z. Ver. Deutsch. Ing.*, 1935, vol. 77, pp. 318–23.
33. K. Zhang, Y.Q. Feng, M.P. Schwarz, Z. Wang, and M. Cooksey: *Ind. Eng. Chem. Res.*, 2013, vol. 52, pp. 11378–90.
34. A. Solheim and J. Thonstad: *Light Metals*, TMS, Warrendale, 1986, pp. 397–403.
35. E. Delnoij, J. Westerweel, J.N. Deen, J.A.M. Kuipers, and W.P.M. van Swaaij: *Chem. Eng. Sci.*, 1999, vol. 54, pp. 5159–71.
36. Y.Q. Feng, M.A. Cooksey, and M.P. Schwarz: *9th Australasian Aluminium Smelting Technology Conf.*, 2007.
37. R.F. Mudde and O. Simonin: *Chem. Eng. Sci.*, 1999, vol. 54, pp. 5061–69.